HHS Public Access

Author manuscript

Cell Rep. Author manuscript; available in PMC 2022 March 09.

Published in final edited form as:

Cell Rep. 2022 February 15; 38(7): 110395. doi:10.1016/j.celrep.2022.110395.

TP53 promotes lineage commitment of human embryonic stem cells through ciliogenesis and sonic hedgehog signaling

Sushama Sivakumar[1,8], **Shutao Qi**[2,3,8], **Ningyan Cheng**[1], **Adwait A. Sathe**[4], **Mohammed Kanchwala**[4], **Ashwani Kumar**[4], **Bret M. Evers**[5], **Chao Xing**[4,6,7], **Hongtao Yu**[1,2,3,9,*]

[1]Department of Pharmacology, University of Texas Southwestern Medical Center, 6001 Forest Park Road, Dallas, TX 75390, USA

[2]Westlake Laboratory of Life Sciences and Biomedicine, Hangzhou, Zhejiang, China

[3]School of Life Sciences, Westlake University, Hangzhou, Zhejiang, China

[4]Eugene McDermott Center for Human Growth and Development, University of Texas Southwestern Medical Center, Dallas, TX 75390, USA

[5]Department of Pathology, University of Texas Southwestern Medical Center, 5323 Harry Hines Boulevard, Dallas, TX 75390, USA

[6]Department of Bioinformatics, University of Texas Southwestern Medical Center, Dallas, TX 75390, USA

[7]Department of Population and Data Sciences, University of Texas Southwestern Medical Center, Dallas, TX 75390, USA

[8]These authors contributed equally

[9]Lead contact

SUMMARY

Aneuploidy, defective differentiation, and inactivation of the tumor suppressor *TP53* all occur frequently during tumorigenesis. Here, we probe the potential links among these cancer traits by inactivating *TP53* in human embryonic stem cells (hESCs). *TP53*$^{-/-}$ hESCs exhibit increased proliferation rates, mitotic errors, and low-grade structural aneuploidy; produce poorly differentiated immature teratomas in mice; and fail to differentiate into neural progenitor cells (NPCs) *in vitro*. Genome-wide CRISPR screen reveals requirements of ciliogenesis and sonic

*Correspondence: yuhongtao@westlake.edu.cn.

AUTHOR CONTRIBUTIONS

S.S. designed and performed all the experiments except those noted below, analyzed data, and wrote the paper. S.Q. performed the genome-wide CRISPR-Cas9 screen and constructed the *IFT140*$^{-/-}$ and *OFD1*$^{-/-}$ hESC lines. N.C. performed TP53 ChIP-seq experiments. A.A.S. and C.X. analyzed RNA-seq and CRISPR-Cas9 data. M.K. and C.X. analyzed ChIP-seq data. A.K. and C.X. analyzed CNV data. B.M.E. assisted with histopathological analysis of teratomas. H.Y. conceived and supervised the study and edited the paper.

SUPPLEMENTAL INFORMATION

Supplemental information can be found online at https://doi.org/10.1016/j.celrep.2022.110395.

DECLARATION OF INTERESTS

The authors declare no competing interests.

hedgehog (Shh) pathways for hESC differentiation into NPCs. *TP53* deletion causes abnormal ciliogenesis in neural rosettes. In addition to restraining cell proliferation through *CDKN1A*, TP53 activates the transcription of *BBS9*, which encodes a ciliogenesis regulator required for proper Shh signaling and NPC formation. This developmentally regulated transcriptional program of TP53 promotes ciliogenesis, restrains Shh signaling, and commits hESCs to neural lineages.

Graphical abstract

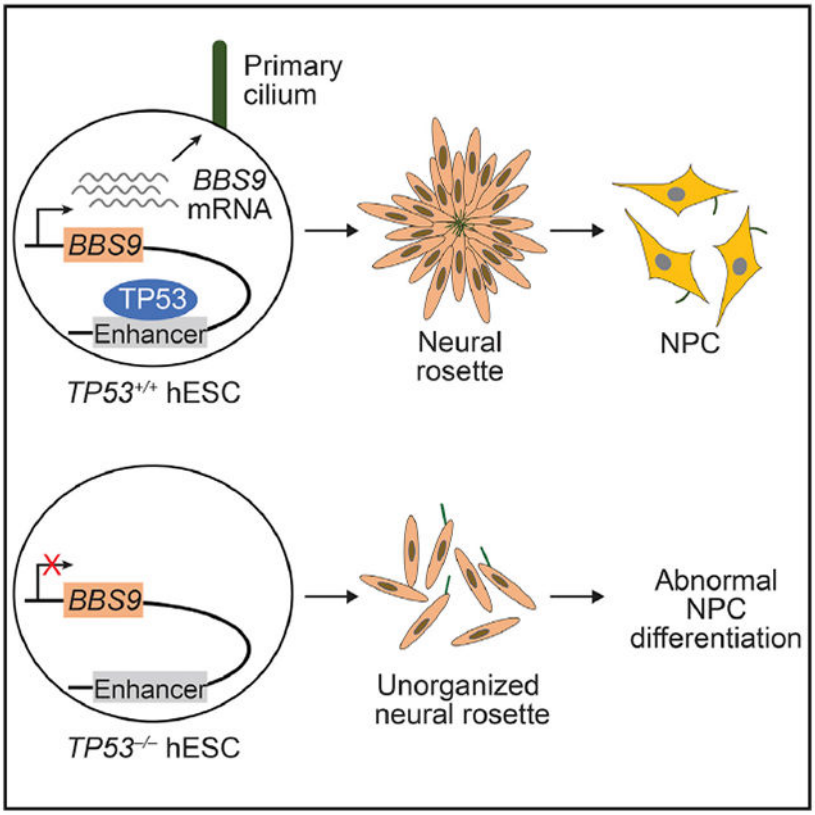

In brief

Sivakumar et al. show that the tumor suppressor TP53 promotes human embryonic stem cell (hESC) differentiation into mature teratomas. They further identify a developmentally regulated transcriptional program of TP53 that promotes ciliogenesis, restrains Shh signaling, and commits hESCs to neural lineages. Their findings implicate the differentiation-promoting function of TP53 in tumor suppression.

INTRODUCTION

Differentiation status is commonly used to classify the grade of solid tumors, with aggressive high-grade tumors being less differentiated or immature and benign low-grade tumors being more differentiated or mature (Amin et al., 2017). The tumor suppressor gene *TP53* is mutated in more than 50% of all human cancers, and tumors with *TP53* mutations have poor differentiation status (Kastenhuber and Lowe, 2017; Stiewe, 2007). Germline

TP53 mutations cause Li-Fraumeni syndrome (LFS), a hereditary cancer syndrome in humans (Malkin et al., 1990). Patients with LFS develop poorly differentiated breast tumors, and induced pluripotent stem cells (iPSCs) derived from LFS patient cells exhibit defective osteoblastic differentiation (Lee et al., 2015). Furthermore, *TP53* and its paralogs *TP63* and *TP73* transcriptionally activate the WNT pathway in human (hESCs) and mouse embryonic stem cells (mESCs) to promote mesendodermal specification (Wang et al., 2017). *TP53* negatively regulates self-renewal of neural and myeloid progenitor stem cells by limiting their proliferation and survival (Lin et al., 2005; Zhao et al., 2010). Finally, *TP53* inhibits reprogramming of differentiated cells into iPSCs (Hong et al., 2009; Kawamura et al., 2009; Marion et al., 2009). Collectively, these findings suggest that TP53 antagonizes the stem cell state and promotes differentiation. By contrast, *Trp53*$^{-/-}$ mice develop normally, although they develop tumors within 6 months of age (Donehower et al., 1992). *TP53*-deficient hESCs have been reported to form teratomas of all three germ layers when injected into mice (Merkle et al., 2017; Song et al., 2010). These findings argue against a requirement for TP53 in development and stem cell differentiation. Therefore, the functions of TP53 in differentiation remain to be further clarified.

Sonic hedgehog (Shh) signaling regulates tissue patterning during embryogenesis, and its aberrant reactivation in differentiated tissue can lead to tumorigenesis (Liu et al., 2018). In mammals, Shh signaling requires the primary cilium wherein receptors and effectors can be concentrated to high levels and potentiate downstream cellular signaling (Goetz and Anderson, 2010). A well-characterized role for Shh signaling is in neural tube formation and patterning (Goetz and Anderson, 2010). Defects in ciliogenesis perturb Shh signaling, resulting in neural tube defects. hESCs have been reported to possess primary cilia, which are enriched for Shh pathway components (Kiprilov et al., 2008).

Aneuploidy is a common trait of tumor cells (Ben-David and Amon, 2020). High-degree aneuploidy is linked to aggressive, metastatic tumors with poor prognosis. The gain of extra chromosomes alters gene dosage and inhibits cell proliferation (Ben-David and Amon, 2020). In contrast, aneuploid tumor cell lines proliferate with high fitness in culture, suggesting that cancer cells might have lost aneuploidy-suppressing mechanisms during tumorigenesis. TP53 mutations are associated with high-degree aneuploidy in human cancers (Pfister et al., 2018), suggesting a role for TP53 in suppressing aneuploidy. Yet, inactivation of *TP53* in cultured diploid or near-diploid cells fails to induce gross aneuploidy (Bunz et al., 2002). These paradoxical findings suggest the existence of selective pressures *in vivo* that allow aneuploid cells to gain higher fitness over their euploid counterparts.

ESCs are prone to develop spontaneous aneuploidy and tend to acquire *TP53* mutations in culture (Merkle et al., 2017; Zhang et al., 2016). Trisomy of single chromosomes in mESCs has been reported to cause increased proliferation rates, decreased differentiation capacity *in vitro*, and the formation of immature teratomas *in vivo* (Zhang et al., 2016). Human teratomas are germ cell tumors that consist of several different tissue types. Virtually all testicular germ cell tumors exhibit aneuploidy (Shen et al., 2018). These findings suggest that aneuploidy might be more tolerated in ESCs.

To understand the origins of aneuploidy, we sought to use teratomas grown from hESCs in mice as an artificial *in vivo* model to evolve aneuploidy. We inactivated *TP53* in hESCs with CRISPR-Cas9 and examined the karyotype, transcriptome, and differentiation of *TP53*-deficient hESCs *in vitro* and using the teratoma assay. Our results indicate that *TP53* loss is insufficient to produce gross whole-chromosome aneuploidy in hESCs or during teratoma formation. Unexpectedly, we discovered that *TP53*-deficient hESCs formed poorly differentiated, immature teratomas and failed to differentiate into functional NPCs *in vitro*. Genome-wide CRISPR-Cas9 screening and subsequent functional studies further link TP53 to ciliogenesis and Shh signaling during NPC formation. Thus, TP53 has an underappreciated role in lineage commitment of hESCs.

RESULTS

TP53$^{-/-}$ hESCs form immature teratomas

We inactivated *TP53* in both H1 and H9 hESCs using CRISPR-Cas9 (Figures 1A and S1A). Among the four *TP53*$^{-/-}$ hESC lines generated, H9 *TP53*$^{-/-}$ clones 1 and 2 (C1 and C2) were derived from single clones, whereas the others were mixed cell populations to avoid clonal bias. The full-length (FL) TP53 protein was absent in all *TP53*$^{-/-}$ hESC lines (Figure 1B). H1 *TP53*$^{-/-}$, H9 *TP53*$^{-/-}$ C1, and H9 *TP53*$^{-/-}$ lines expressed truncated forms of TP53, namely, ΔN40 or ΔN133 TP53 (Aoubala et al., 2011; Courtois et al., 2002). These truncated forms of TP53 are functionally deficient, because they lack the intact transactivation domain (TAD) (Figure 1A). The *TP53*$^{-/-}$ hESCs maintained the expression of pluripotency markers NANOG, SOX2, and OCT3/4 based on flow cytometry and immunofluorescence (Figures 1C and S1B).

The *TP53*$^{-/-}$ hESCs proliferated faster than wild-type (WT) hESCs (Figure 1D). *TP53*$^{-/-}$ hESCs had larger nuclear and cell sizes and mitotic errors (Drost et al., 2015) (Figures S1C–S1G). Despite these phenotypes, *TP53*$^{-/-}$ hESCs in culture had the normal diploid karyotype and did not display prevalent whole-chromosome aneuploidy (Table S1). Some *TP53*$^{-/-}$ hESCs exhibited arm-level copy number variations (CNVs) in certain chromosomes. Thus, TP53 loss is insufficient to induce whole-chromosome aneuploidy in hESCs but permits arm-level CNVs.

When injected into immunodeficient mice, hESCs develop into teratomas that contain cells from all three germ layers (Solter, 2006). To test the pluripotency of *TP53*$^{-/-}$ hESCs, we injected WT and *TP53*$^{-/-}$ hESCs subcutaneously into immunodeficient NOD-SCID mice. Macroscopically, the WT teratomas contained multiple fluid-filled cysts, while the *TP53*$^{-/-}$ teratomas were solid tumors (Figure S2A). Histological analysis revealed that the WT teratomas were composed of large cysts lined with mature, well-differentiated cells, as well as other mature tissues, belonging to all three germ layers (Figure S2B). By contrast, the *TP53*$^{-/-}$ teratomas were predominately composed of sheets of poorly differentiated cells with high nuclear-to-cytoplasmic (NC) ratio. Quantification confirmed that WT teratomas indeed consisted mostly of mature elements, while *TP53*$^{-/-}$ teratomas contained high percentages of poorly differentiated, immature elements (Figures 1E and 1F). Large neural rosette (NR)-like structures formed by poorly differentiated neural cells were frequently observed in *TP53*$^{-/-}$ teratomas (Figure 1E).

WT teratomas contained many ciliated cells and few mitotic cells (Figures 2A and S3A). The *TP53*$^{-/-}$ teratomas, however, lacked ciliated cells and exhibited higher mitotic indices. Expression of the mature element marker glial fibrillary acidic protein (GFAP) was decreased in *TP53*$^{-/-}$ teratomas, while expression of SALL4 and Glypican-3, which are markers for immature elements, was increased (Figure S3B). Our results show that, contrary to a previous report (Song et al., 2010), deletion of *TP53* impairs differentiation of hESCs in teratomas *in vivo*. Whole-genome sequencing (WGS) revealed that these poorly differentiated *TP53*$^{-/-}$ teratomas did not exhibit gross whole-chromosome aneuploidy, indicating that TP53 loss is insufficient to induce aneuploidy during teratoma formation.

TP53$^{-/-}$ hESCs are deficient in differentiation into neural lineages

We next compared the gene expression profiles of WT and H9 *TP53*$^{-/-}$ teratomas. About 3,000 differentially expressed genes (DEGs) were identified between WT and *TP53*$^{-/-}$ teratomas, indicative of global gene expression changes. Tissue-specific enrichment analysis (TSEA) showed that the top 200 DEGs were enriched for genes specifically expressed in the brain (Figure S3C). Pathway analysis of the DEGs revealed that the cilium pathway was downregulated in *TP53*$^{-/-}$ teratomas, whereas neurogenesis and neuron differentiation were among the top upregulated pathways (Figure 2B). Heatmap of the top 200 DEGs revealed that multiple ciliary genes and numerous neurogenesis genes were downregulated and upregulated, respectively, in *TP53*$^{-/-}$ teratomas (Figure 2C). The gene expression changes are consistent with the histological observation that *TP53*$^{-/-}$ teratomas lacked cilia and were enriched for immature neural elements.

To probe the functions of TP53 in neural differentiation, we performed an *in vitro* differentiation assay of hESCs using the 3D embryoid body (EB) protocol (Figure S4A). In this assay, hESCs are first plated in microwells to form EBs. The EBs are plated in monolayers to form NRs, a radial arrangement of cells representative of the neural tube stage in embryonic development (Deglincerti et al., 2016; Elkabetz et al., 2008). NRs are then isolated and induced to produce neural progenitor cells (NPCs). We analyzed the ability of WT and *TP53*$^{-/-}$ hESCs to form EB, NRs, and NPCs during differentiation. Both WT and *TP53*$^{-/-}$ hESCs formed EBs efficiently, with *TP53*$^{-/-}$ EBs being slightly smaller than WT EBs (Figures S4B and S4C).

WT EBs produced well-organized NRs, as evidenced by the radial arrangement of the tight junction protein ZO-1, which redistributed to the apical side of NRs during differentiation (Elkabetz et al., 2008) (Figure 3A). Another feature of mature NRs is the generation and organization of primary cilia in the apical region (He et al., 2014). WT NRs contained radial arrays of cilia with their tips pointing toward the apical lumen (Figures 3B and 3C). *TP53*$^{-/-}$ EBs were severely impaired in NR organization. The total differentiated areas of *TP53*$^{-/-}$ NRs were greatly decreased (Figures S4D and S4E). Expression of the NR marker PAX6 was deficient in *TP53*$^{-/-}$ NRs (Figure S4F). *TP53*$^{-/-}$ NRs were disorganized, as evidenced by the incomplete ZO-1 redistribution to the apical region and disordered arrays of acetylated tubulin and cilia (Figures 3A–3C). The number of radial arrangements in each *TP53*$^{-/-}$ NR was also reduced (Figure 3D).

WT NRs efficiently differentiated into NPCs that expressed SOX1, SOX2, and NESTIN (Figures 3E and S4G–J). Differentiation of *TP53*$^{-/-}$ NRs into NPCs was defective, because *TP53*$^{-/-}$ NPCs displayed greatly reduced expression of SOX1, SOX2, and NESTIN. The NPC-like cells derived from *TP53*$^{-/-}$ NRs were still capable of proliferation and expressed the proliferation marker KI67 (Figures S5A and S5B). *TP53*$^{-/-}$ NPCs were functionally defective, because they failed to differentiate into neurons or astrocytes (Figures S5C and S5D).

We compared the gene expression profiles of NPCs derived from three H9 *TP53*$^{-/-}$ hESC lines with their respective WT controls. Pairwise comparisons revealed 1,660 DEGs between NPCs derived from H9 WT and *TP53*$^{-/-}$ C1, 3,113 DEGs between H9 WT and *TP53*$^{-/-}$ C2, and 2,131 DEGs between H9 LC and the *TP53*$^{-/-}$ pool (Figure S6A). We reasoned that common DEGs found in all three pairwise comparisons might be less likely influenced by the genomic instability caused by TP53 loss and capture the genuine differentiation defects in *TP53*$^{-/-}$ NPCs. Only 589 DEGs were common among all three pairwise comparisons.

The heatmap of expression levels of these 589 common genes showed that multiple genes involved in neuron differentiation were downregulated, whereas genes involved in cell proliferation were upregulated in *TP53*$^{-/-}$ NPCs (Figure S6B). Pathway analysis confirmed that the top downregulated pathways were integral to neuronal functions and differentiation (Figure 3F). The top upregulated pathways included cell proliferation, biological adhesion, cellular component movement, and tube development. Thus, *TP53*$^{-/-}$ NPCs are deficient in the expression of genes required for neuronal differentiation.

TP53 occupies neurogenesis genes in hESCs

Although TP53 loss did not cause gross aneuploidy in ESCs, it did create genomic instability, including arm-level aneuploidy, which was different in each *TP53*$^{-/-}$ hESC line. Indeed, karyotype analysis revealed that about 20% of NPCs derived from two different *TP53*$^{-/-}$ hESC lines retained the corresponding original structural aneuploidy in the ESC state (Table S1). Multiple *TP53*$^{-/-}$ hESC lines retained the corresponding original structural aneuploidy in the ESC state hESCs with distinct chromosomal abnormalities and genetic mutations exhibited similar differentiation defects in the teratoma and *in vitro* differentiation assays. Expression of the WT *TP53* transgene in H9 *TP53*$^{-/-}$ C2 hESCs restored SOX1 and SOX2 expression in the NPC state (Figures 3G, S4G, and S4H). Therefore, the genomic instability unleashed by TP53 loss is not solely responsible for the differentiation defects. As a transcription factor, TP53 might directly or indirectly promote the transcription of cell fate determination genes, including *SOX1* and *SOX2*.

To identify direct transcription targets of TP53, we performed chromatin immunoprecipitation (ChIP) followed by next-generation sequencing (ChIP-seq) analysis in WT hESCs and NPCs. *De novo* motif search identified the TP53-binding consensus in the enriched peaks in both hESCs and NPCs (Figure 3H). About 76% of the chromosome loci occupied by TP53 in the stem cell state remained occupied by TP53 in the NPC state (Figures 3I and S6C). Pathway analysis of genes occupied by TP53 in hESCs unexpectedly reveals the enrichment of genes in neurogenesis and neuron differentiation pathways (Figure 3J), aside from the expected enrichment of genes in the canonical TP53

pathways. This surprising finding suggests that TP53 already occupies genes required for neuronal differentiation in the stem cell state.

RNA-seq analysis showed that 106 DEGs were common among pairwise comparisons between three different *TP53*$^{-/-}$ hESCs and their corresponding WT controls (Figure S6D). The expression heatmap of the common 106 DEGs showed that multiple genes involved in the TP53 pathway were downregulated, whereas genes involved in cell proliferation were upregulated (Figure S6E). Pathway analysis of these DEGs identified the canonical TP53 pathways but did not show enrichment of neurogenesis genes (Figure S6F). Despite being occupied by TP53 in hESCs, several known regulators of neuronal functions, including *SYT1* and *SLITRK1*, were not differentially expressed between WT and *TP53*$^{-/-}$ hESCs. By contrast, 54% of the TP53-occupied genes in NPCs were differentially expressed between WT and *TP53*$^{-/-}$ NPCs. Thus, TP53 already occupies neuronal genes at the stem cell state and is poised to activate their expression during NPC differentiation.

Genome-wide screen reveals requirement for ciliogenesis and Shh signaling during NPC differentiation

To functionally link TP53 target genes to differentiation, we performed a genome-wide CRISPR-Cas9 screen to identify genes required for NPC differentiation. RNA-seq analysis revealed that the well-established NPC marker *SOX1* was the top DEG between WT hESCs and NPCs (Figure S7A). We used SOX1 as the surrogate marker for NPCs (Figure 4A). WT hESCs were infected with the lentiviral human GeCKOv2 library and induced to undergo NPC differentiation by the monolayer protocol (Chambers et al., 2009). We collected the 1% of cells with lowest SOX1 expression from the differentiated cell population using flow cytometry. The single-guide RNAs (sgRNAs) enriched in these SOX1^{-} cells were thus expected to target genes required for NPC differentiation. *SOX1* was a top hit from the screen, confirming its validity (Figure 4B). Other top hits included genes involved in ciliogenesis and negative regulators of Shh signaling (Figures 4B and 4C). Our screen was not saturated, because *TP53* was not identified in the screen.

The ciliary genes *IFT140* and *OFD1* were among the top hits in our screen. IFT140 is a core subunit of the IFT-A subcomplex, which is required for retrograde transport within the primary cilium (Picariello et al., 2019). OFD1 is required for ciliogenesis and neuronal patterning in mice (Ferrante et al., 2006; Hunkapiller et al., 2011). We generated hESCs with *IFT140* and *OFD1* individually deleted (Figure S7B). About 30% of WT hESCs possessed primary cilia (Figures S7C and S7D). Deletion of *IFT140* or *OFD1* abolished ciliogenesis in hESCs. Strikingly, when injected into mice, *IFT140*$^{-/-}$ and *OFD1*$^{-/-}$ hESCs formed highly immature teratomas with numerous disorganized, less compact NRs (Figures 4D and S7E). Similar to *TP53*$^{-/-}$ teratomas, *IFT140*$^{-/-}$ and *OFD1*$^{-/-}$ teratomas exhibited greatly reduced SOX1 expression (Figure 4E). Ciliogenesis in NRs of *IFT140*$^{-/-}$ and *OFD1*$^{-/-}$ teratomas was severely compromised (Figure S7F). Similar defects in NR organization, ciliogenesis, and SOX1 expression were also observed for *IFT140*$^{-/-}$ and *OFD1*$^{-/-}$ hESCs during *in vitro* differentiation (Figures 5A–5D). Our results suggest that ciliogenesis promotes the formation of tightly compacted NRs, which are critical for differentiation toward neuronal lineages.

The GLI proteins are effectors of the Hedgehog pathway, and primary cilia are required for the formation of both GLI activator and repressor forms (Bangs and Anderson, 2017). Mutations of *IFT* genes disrupt primary cilia formation and inhibit GLI3 processing to its repressor form (Huangfu and Anderson, 2005; Liu et al., 2005; May et al., 2005). mESCs with *OFD1* mutations lack primary cilia and display reduced processing of FL GLI3 to repressor form of GLI3 (GLI3R) during differentiation (Hunkapiller et al., 2011). We examined the status of Shh signaling and GLI protein processing during differentiation to NPCs. Shh signaling was downregulated during the differentiation of WT hESCs to NPCs, as evidenced by decreased protein levels of GLI1 and GLI3 FL and the accumulation of the cleaved GLI3R (Figure 5E). Consistent with well-established roles of primary cilia in regulating Shh signaling, *IFT140*$^{-/-}$ and *OFD1*$^{-/-}$ NPCs (which lacked primary cilia) had elevated levels of GLI1 and GLI3 FL and decreased levels of GLI3R (Figure 5E), indicating a failure to downregulate Shh signaling.

Because primary cilia are required for GLI3 processing, reduced processing of GLI3 FL to GLI3R in *IFT140*$^{-/-}$ and *OFD1*$^{-/-}$ NPCs is likely caused by the ciliogenesis defect. In contrast, increases in GLI1 protein levels in the absence of primary cilia in *IFT140*$^{-/-}$ EBs and NPCs suggest that this can occur in a cilia-independent manner. Thus, during hESC differentiation, primary cilia are required for the formation of organized NRs where GLI3 is processed to GLI3R to allow *SOX1* expression and NPC differentiation.

BBS9 is a TP53 target gene that regulates ciliogenesis and NPC differentiation

We tested whether the NPC differentiation defects of *TP53*$^{-/-}$ hESCs were linked to defective ciliogenesis and dysregulated Shh signaling. *TP53*$^{-/-}$ hESCs were deficient in ciliogenesis (Figures 5F and 5G). This defect was partially rescued by re-expressing WT *TP53*. The disorganized NRs formed by *TP53*$^{-/-}$ hESCs during NPC differentiation displayed reduced cilia formation (Figures S8A and S8B). Similar to *IFT140*$^{-/-}$ and *OFD1*$^{-/-}$ cells, *TP53*$^{-/-}$ EBs and NPC-like cells exhibited increased *GLI1* mRNA and GLI1 protein levels and decreased GLI3R levels (Figures S8C and 5H), consistent with unrestrained Shh signaling. *TP53*$^{-/-}$ NRs exhibited modest ciliogenesis defects, which might account for the partial processing of GLI3 FL to GLI3R (Figure 5H). Thus, ciliogenesis and Shh signaling are perturbed in *TP53*$^{-/-}$ hESCs during differentiation.

TP53 occupies neurogenesis genes in the stem cell state, suggesting that it might promote commitment to neural lineages at the onset of differentiation. Among common DEGs between WT and *TP53*$^{-/-}$ hESCs, 18 of them contained TP53 peaks in the ChIP-seq data of both hESCs and NPCs (Figures 6A and 6B), suggesting that they might be direct TP53 target genes throughout the differentiation process. The list of these 18 genes included the best-characterized TP53 target gene *CDKN1A* (Figure 6B), which encodes a cyclin-dependent kinase inhibitor that arrests the cell cycle in response to various stimuli (Abbas and Dutta, 2009). Strikingly, the list also included the Bardet-Biedl syndrome 9 (*BBS9*) and patched domain-containing protein 4 (*PTCHD4*) genes. *BBS9* encodes a core subunit of the BBSome, which regulates IFT assembly and transport within the cilia (Wei et al., 2012). *PTCHD4* encodes a negative regulator of Shh signaling with homology to PTCH1 (Chung et

al., 2014). *BBS9* and *PTCHD4* are thus candidate TP53 target genes with direct functions in ciliogenesis and Shh signaling.

PTCHD4 has already been shown to be a TP53 target gene whose overexpression negatively regulates Shh signaling (Chung et al., 2014). We decided to further characterize *BBS9*. Quantitative RT-PCR confirmed that, similar to *CDKN1A*, expression of *BBS9* was decreased in $TP53^{-/-}$ hESCs, EBs, and NPCs (Figure 6C). Based on ChIP-seq, TP53 binds to introns 9 and 14 within the *BBS9* gene (Figure 6D). The TP53-binding site in intron 14 (termed TP53BS1) contains a TP53-binding consensus motif. TP53BS1 likely represents an enhancer, because this genomic region is enriched for the enhancer marker H3K27ac and exhibits increased chromatin accessibility (Figure 6D) (GSM2386581, GSM1521726) (Ziller et al., 2015). Strikingly, deletion of TP53BS1 in *BBS9* ($BBS9^{\Delta TP53BS1}$) greatly reduced mRNA and protein levels of *BBS9* in both ESCs and NPCs (Figures 6E, 6F, and S9A). *In-vitro*-differentiated $TP53^{-/-}$ NPCs showed reduced BBS9 protein levels (Figure 6F). These findings indicate that TP53 promotes the expression of *BBS9* by binding to an enhancer element in the *BBS9* gene body.

We next generated H9 $BBS9^{-/-}$ hESCs (Figure S9A). Because of the intimate connection between cell proliferation and differentiation, we also created hESCs with *CDKN1A* deleted or with both *BBS9* and *CDKN1A* deleted. Both $BBS9^{-/-}$ and $BBS9^{\Delta TP53BS1}$ hESCs displayed reduced ciliogenesis (Figures 7A and 7B). During differentiation, $BBS9^{-/-}$ and $BBS9^{\Delta TP53BS1}$ hESCs formed disorganized NRs with defective ciliogenesis (Figures 7C, 7D, S9B, and S9C). $BBS9^{-/-}$ and $BBS9^{\Delta TP53\text{-}BS1}$ EBs and NPCs exhibited elevated GLI1 protein levels and decreased GLI3R and SOX1 levels (Figure 7E). Thus, TP53 promotes the expression of *BBS9* to regulate ciliogenesis and Shh signaling during the differentiation of hESCs into NPCs.

$CDKN1A^{-/-}$ hESCs expectedly proliferated faster than WT hESCs (Figure S9D) but did not exhibit ciliogenesis defects (Figures 7A and 7B). Deletion of *CDKN1A* alone did not affect NR formation or reduce SOX1 protein levels in NPCs (Figures 7C, 7D, and S9E). When injected into mice, $CDKN1A^{-/-}$ hESCs formed well-differentiated teratomas, indicating that the increased proliferation per se was insufficient to induce differentiation defects (Figure S9F). In contrast, deletion of both *BBS9* and *CDKN1A* exacerbated the NR formation defects caused by single *BBS9* deletion (Figures 7C and 7D). $BBS9^{-/-}/CDKN1A^{-/-}$ NPCs had much lower SOX1 expression than $BBS9^{-/-}$ NPCs (Figure 7E). These results indicated that *CDKN1A* contributes to NPC differentiation in cells lacking *BBS9*. Deletion of both *BBS9* and *CDKN1A* did not cause more severe ciliogenesis defects than *BBS9* single deletion did (Figures 7C and 7D), suggesting that *CDKN1A* promotes NPC differentiation in pathways independent of ciliogenesis.

DISCUSSION

When studying genomic instability in teratomas, we unexpectedly discovered a requirement for TP53 in hESC differentiation. Genetic analyses link TP53 to ciliogenesis and Shh signaling during differentiation into NPCs and identify *BBS9* as a critical TP53 target gene in this process.

Functions of TP53 in differentiation

We used the teratoma assay to understand how TP53 regulates differentiation. The teratoma assay is a promising platform to study early human development (McDonald et al., 2020). We showed that, despite proper expression of stem cell markers, *TP53*$^{-/-}$ hESCs formed highly immature teratomas with high NC ratio, increased mitotic index, and reduced ciliogenesis.

This finding was unexpected, because two previous studies had reported that TP53-deficient hESCs could form mature teratomas (Merkle et al., 2017; Song et al., 2010). The underlying reasons for this discrepancy are unclear but could be because of multiple factors. First, the extent of TP53 inactivation varies among studies. In one of the two previous studies (Merkle et al., 2017), hESCs harboring spontaneous point mutations of TP53 were examined. These point mutations do not completely inactivate TP53. By contrast, the *TP53*$^{-/-}$ hESC lines used in our study harbor nearly complete loss of function of TP53 mutations. Second, even a nearly complete inactivation of TP53 produces phenotypes of incomplete penetrance and high variance among individual teratomas (Figure 1F). The limited numbers of TP53-deficient cell lines and teratomas used in previous studies might have prevented the detection of these phenotypes. The advent of CRISPR-Cas9 allowed us to construct multiple *TP53*$^{-/-}$ cell lines. Automated image acquisition enabled broad sampling and rigorous quantification of large histological staining sections of tens of teratomas. Our results convincingly show that *TP53*$^{-/-}$ hESCs are deficient in differentiation and form highly immature teratomas.

In vitro differentiation assays confirm a role of TP53 in neural differentiation. TP53 occupies neurogenesis genes even in the stem cell state, suggesting that it is poised to promote neurogenesis. In contrast, the differentiation functions of TP53 are not limited to neural lineages, because TP53 loss causes differentiation defects in other lineages in teratomas. A prior study found that decreased expression of TP53 using RNAi leads to increased neuronal differentiation and reduced proliferation rate in both human neuroepithelial cells and brain organoids (Marin Navarro et al., 2020). In our study, we have completely ablated TP53 expression using CRISPR-Cas9 in the stem cell state and then differentiated ESCs into NPCs. Differences in cell lines and differentiation protocols may account for some of the differences between the two studies.

Depletion of TP53 in *Xenopus laevis* and zebrafish causes defects in embryogenesis (Cordenonsi et al., 2003). Although most *Trp53*$^{-/-}$ mice develop to term normally, 25% of female *Trp53*$^{-/-}$ mice die during embryogenesis because of defects in neural tube closure (Armstrong et al., 1995). This subtle defect in mice might be more easily distinguishable in our targeted *in vitro* neuronal differentiation assay. Thus, the function of TP53 in early development is evolutionarily conserved. In *Trp53*$^{-/-}$ mice, the TP53 homologs, TP63 and TP73, compensate for TP53 loss (Molchadsky et al., 2010), explaining their subtle developmental phenotypes. For unknown reasons, TP63 and TP73 cannot effectively compensate for TP53 loss in hESCs, revealing a requirement for TP53 in differentiation.

Mechanisms by which TP53 promotes differentiation

Although *TP53* deletion does not cause whole-chromosome aneuploidy in hESCs, it induces CNVs at the chromosome arm level (Table S1) (Soto et al., 2017). Moreover, *TP53*$^{-/-}$ hESCs likely harbor additional small genetic alterations and mutations. The genomic instability caused by TP53 loss might contribute to the differentiation defects of *TP53*$^{-/-}$ hESCs. In contrast, multiple cell lines with different CNVs and presumably other genetic alterations exhibit similar differentiation defects. Re-expression of the *TP53* transgene in *TP53*$^{-/-}$ hESCs, which does not revert the genetic changes, alleviates the differentiation defects. These findings argue against the possibility that differentiation defects of *TP53*$^{-/-}$ hESCs are passive, secondary consequences of genomic instability.

Our subsequent findings suggest that TP53 uses multifaceted mechanisms to actively promote hESC differentiation (Figure 7F). TP53 maintains the transcription of *CDKN1A* in all cellular states. As a critical CDK inhibitor, CDKN1A restrains the G1/S transition during the cell cycle to favor differentiation. In addition, TP53 induces the transcription of *BBS9* and *PTCHD4*, whose expression is required for proper ciliogenesis and Shh signaling during NR formation. Collectively, this TP53-orchestrated transcriptional program coordinates cell division, ciliogenesis, and Shh signaling to promote differentiation.

As a conserved microtubule-based organelle, the primary cilium is critical for transducing signals from the external environment to regulate key cellular processes, including cell polarity, differentiation, and proliferation (Goetz and Anderson, 2010). An important function of primary cilia is to regulate Shh signaling. Our genome-wide CRISPR-Cas9 screen reveals a requirement for ciliogenesis genes and negative regulators of Shh signaling in the differentiation of hESCs into NPCs. Inactivation of ciliogenesis genes, including those identified in our screen, causes developmental defects in mouse and other model organisms (Ferrante et al., 2006; Hunkapiller et al., 2011). Their mutations are linked to multi-system developmental syndromes termed ciliopathies in humans (Schmidts et al., 2013; Zaghloul and Katsanis, 2009). Our findings extend the role of ciliogenesis and Shh signaling to the differentiation of hESCs into neural lineages and establish TP53 as a key coordinator of NR formation (Figure 7F).

Contrary to our results, a prior study found that mESCs with *Ofd1* mutated exhibit increased *Sox1* expression during early differentiation (Hunkapiller et al., 2011). However, similar to *OFD1*$^{-/-}$ hESCs and NPCs in our study, these *Ofd1* mutant mESCs exhibit ciliogenesis and GLI3 processing defects. We speculate that the differences in *SOX1* expression during neuronal differentiation may be because of interspecies variations.

Only 30% of cultured hESCs form primary cilia. On induction of neuronal differentiation, primary cilia can be observed on the apical side of NRs and in the majority of NPCs. Deletion of *IFT140* and *OFD1* abolishes primary cilia formation in hESCs, NRs, and NPCs. Inactivation of *TP53* or its transcription target *BBS9* also compromised ciliogenesis in hESCs and NRs. In all cases, defective ciliogenesis leads to disorganized NRs and elevated GLI1 levels and incomplete GLI3R processing, indicative of unrestrained Shh signaling. The requirement of primary cilia for efficient processing of GLI3 FL into GLI3R is consistent with findings in the mouse (Huangfu and Anderson, 2005; Liu et al., 2005; May et al.,

2005). Our attempts to rescue differentiation defect in *TP53*$^{-/-}$ hESCs using chemical inhibitors of Shh signaling were not successful, suggesting that the differentiation defects of these cells are not simply due to hyperactive Shh signaling. Alternatively, it might be difficult to restore the proper spatiotemporal dynamics of Shh signaling in *TP53*$^{-/-}$ hESCs with the use of chemical inhibitors.

The graded hedgehog signaling response controls dorsal-ventral patterning in the developing mouse neural tube and relies on a gradient of GLI activity (Stamataki et al., 2005). Small perturbations of GLI levels can alter the proper development of distinct cell types. NRs with their apical-basal polarity bear resemblance to the nascent neural tube. Ciliogenesis occurs only on the apical side of NRs, forming dense radial arrays of primary cilia with their tips pointing into the lumen. We propose that this high-density, ordered arrangement of cilia ensures proper Shh signaling and cell lineage specification in NRs (Figure 7F). Loss of TP53 or its downstream target genes, such as *BBS9*, reduces the density of primary cilia and perturbs their organization and function. TP53 further inhibits Shh signaling by promoting the expression of *PTCHD4*, which encodes a negative regulator of Shh signaling. Collectively, TP53 deficiency leads to aberrantly elevated Shh signaling and defective NPC formation.

Tumor suppression by TP53

TP53 responds to genotoxic and oxidative stresses and activates distinct transcriptional programs to elicit cell-cycle arrest, apoptosis, and ferroptosis, thereby suppressing tumorigenesis. Our study identifies a developmentally regulated transcriptional program of TP53 under basal conditions and links TP53 to ciliogenesis and the control of Shh signaling. Perturbation of this program prevents lineage commitment and produces poorly differentiated immature elements. Poor differentiation is a universal feature of malignant tumors of different tissue origins. Ciliogenesis is generally suppressed during tumorigenesis (Goetz and Anderson, 2010). Aberrant activation of Shh signaling has been observed in several human tumors, particularly in medulloblastomas and basal cell carcinoma (Briscoe and Therond, 2013). In a subset of medulloblastomas, the lack of primary cilia reduces GLI3R levels, resulting in abnormal activation of Shh signaling and aggressive tumors (Bangs and Anderson, 2017; Han et al., 2009). These findings raise the intriguing possibility that the differentiation-promoting functions of TP53 might contribute to tumor suppression.

Limitations of the study

Teratomas grown from hESCs in heterologous hosts recapitulate early events of human embryogenesis and provide a model for understanding human teratomas. Even though *TP53* loss in hESCs produces immature teratomas in the mouse, both mature and immature teratomas in human patients rarely contain *TP53* mutations. In this study, the functions of TP53 in differentiation were characterized using *in vitro* systems. Whether this developmentally regulated transcriptional program of TP53 identified *in vitro* is dysfunctional in immature human teratomas needs future investigations. *TP53* mutations in human cancers typically do not involve the complete loss of function of both alleles. It will be interesting to test whether hESCs engineered to harbor *TP53* missense mutations in human cancers exhibit differentiation defects in teratomas and human organoids.

Human LFS patients, who have germline *TP53* mutations, are susceptible to developing cancers in multiple tissues (Malkin et al., 1990). Future experiments are needed to test whether differentiation defects of stem/progenitor cells caused by TP53 deficiency contribute to tumorigenesis in LFS patients and, more broadly, whether dysfunction of the developmentally regulated transcriptional program of TP53 contributes to poor differentiation of human cancers driven by TP53 inactivation.

STAR★METHODS

RESOURCE AVAILABILITY

Lead contact—Further information and requests for reagents should be directed to and will be fulfilled by the lead contact, Hongtao Yu (yuhongtao@westlake.edu.cn).

Materials availability—All reagents generated in this study are available upon request from the lead contact, Hongtao Yu (yuhongtao@westlake.edu.cn).

Data and code availability

- All raw and analyzed next-generation sequencing data, including RNA-seq, ChIP-seq, and CRISPR-Cas9 screen data, have been deposited to the NCBI GEO. These data are publicly available as of the date of publication. Accession numbers are provided in the Key Resources Table.
- This paper does not report original code.
- Any additional data and information required to analyze the data reported in this paper are available from the lead contact upon request.

EXPERIMENTAL MODEL AND SUBJECT DETAILS

Mice—NOD SCID mice were purchased from UT Southwestern breeding core or from The Jackson laboratory. All mice were housed in specific pathogen free barrier facility at UT Southwestern Medical center. Female mice between 6 and 8 weeks of age were used to do teratoma assay. All mice experiments were performed in accordance with institutional guidelines and with approval from the institutional animal care and use committee at UT Southwestern Medical Center.

Cell lines—Human embryonic stem cell lines (H1/WA01 and H9/WA09) were obtained from Wicell Research Institute. The cell lines were routinely tested and only used when free of mycoplasma contamination. All human stem cell work described in this manuscript has been conducted under the oversight of the Stem Cell Research Oversight (SCRO) Committee at UT Southwestern Medical Center.

METHOD DETAILS

Cell culture and gene editing—Human embryonic stem cells (hESCs) (H1/WA01 and H9/WA09) were purchased from WiCell Research Institute, Wisconsin, USA. The hESCs were cultured under feeder-free conditions in mTeSR1-cGMP media on plates coated with

Matrigel (Corning). Versene (Thermo Fisher Scientific) was used to passage hESCs. The hESCs were routinely tested for mycoplasma to avoid any contamination.

For the generation of *TP53*$^{-/-}$ hESCs, sgRNAs targeting exons 2 or 4 of *TP53* were cloned into px458-GFP, px459-puro, or pLenti-Cas9 plasmids (obtained from Addgene)(Ran et al., 2013). SgRNA sequences can be found in the Key Resources Table. The px458/px459 plasmids were transfected into hESCs with electroporation using the Lonza 4D-Nucleofector according to the manufacturer's instructions. One day after electroporation, cells were selected either by flow cytometry (FACS) for GFP expression or by treatment with 1 μg/mL puromycin. Selected cells were allowed to grow into colonies, which were then isolated to obtain the H9 *TP53*$^{-/-}$ C1 cell line. A population of selected cells was used for the H1 *TP53*$^{-/-}$ cells. For the packaging of lentiviruses, pLenti-Cas9 plasmids (with the *TP53* sgRNAs or without an sgRNA) along with pMD2.G and psPAX2 were transfected into HEK293FT cells using Lipofectamine 2000 (Life Technologies). Viral supernatants were collected at 2-3 days after transfection, concentrated using Lenti X concentrator (Clontech), and added to H9 hESCs growing on Matrigel along with 4 μg/mL polybrene. The infected cells were selected with 1 μg/mL puromycin. The surviving clones were picked to obtain the H9 *TP53*$^{-/-}$ C2 cell line. A population of surviving cells was collected and referred to as H9 *TP53*$^{-/-}$ to avoid clonal bias. Surviving cells from H9 hESCs infected with the lentivirus without sgRNAs were used as H9 WT lentivirus controls (referred to as H9 WT LC). The loss of TP53 in the knockout cell lines was verified by Western blotting and DNA sequencing of the *TP53* alleles.

H9 *IFT140*$^{-/-}$ OFD1$^{-/-}$, *CDKN1A*$^{-/-}$ and *BBS9*$^{-/-}$ clonal hESC lines were generated using the lentivirus procedure as described above using guides listed in the Key Resources Table. The *CDKN1A*$^{-/-}$ hESC line was further infected with the lentivirus containing sgRNAs targeting *BBS9* (BBS9 sgRNA#1 and sgRNA#2 from the Key Resources Table) to generate the *CDKN1A*$^{-/-}$/*BBS9*$^{-/-}$ hESC clonal cell line.

All stem cell work described in this manuscript has been conducted under the oversight of the Stem Cell Research Oversight (SCRO) Committee at UT Southwestern Medical Center. When establishing stem cell research standards, UT Southwestern follows the International Society for Stem Cell Research (ISSCR) guidelines for stem cell research and clinical translation and National Institutes of Health guidelines for human stem cell research.

Cell proliferation assay and flow cytometry—WT, *TP53*$^{-/-}$, and *CDKN1A*$^{-/-}$ hESCs were plated in triplicates on Matrigel-coated plates. At 24-h intervals, cells were dissociated, stained with Trypan blue, and counted using a Bio-Rad TC20 automated cell counter. For flow cytometry, hESCs were fixed with 2-4% PFA, permeabilized with methanol, and then stained with anti-SOX2 (APC; Miltenyi Biotec), anti-OCT3/4 (PE; Miltenyi Biotec), and anti-NANOG (BV421; BioLegend) antibodies and DAPI. Cells were analyzed using a Beckman Coulter CytoFLEX flow cytometer.

Giemsa (G) banding and karyotyping—hESCs and NPCs (differentiated by the 3D embryoid body protocol) were grown in Matrigel-coated or regular 25 cm^2 tissue culture flasks with the appropriate media. The live cells in culture flasks were shipped to WiCell

Research Institute for G banding and karyotyping. For reversine treatment, hESCs were treated with 1 μM reversine for 48 h. After reversine was washed off, the surviving cells were allowed to recover in culture for 2 weeks before being sent to WiCell for G banding analysis.

Live-cell imaging—hESCs were grown in Matrigel-coated Nunc Lab-Tek chambered coverglass (Thermo Fisher Scientific; cat#155411). Aphidicolin was added at 200 ng/mL for 12 h to synchronize cells in the G1 phase. Before imaging, the cell-permeable Hoechst 33342 dye (Life Technologies) was added to cells at 10–50 ng/mL. Images were captured at 5-min intervals for 10–18 h using a 40X objective and an Evolve 512 Delta EMCCD camera on a Leica inverted microscope equipped with an environmental chamber that controls temperature and CO_2. Time-lapsed videos displaying elapsed times between consecutive frames were assembled using the MetaMorph Software (MDS Analytical Technologies) and analyzed using ImageJ. The mitotic duration between nuclear envelope breakdown and anaphase onset was manually determined for each cell. Mitotic defects were visually identified and counted. GraphPad Prism was used to generate the scatter plots and stacked bar graphs.

Immunofluorescence—hESCs were grown on Matrigel-coated coverslips. Cells were fixed with the 4% paraformaldehyde solution containing 0.5% Triton X-100. Fixed cells were incubated with the blocking solution (3% BSA in PBS containing 0.1% Tween 20) for 1 h. Cells were then treated with primary antibodies diluted in the blocking solution and incubated overnight at 4C. Primary antibodies used for staining included anti-ZO-1 (Invitrogen), anti-SOX2 (Abcam), anti-NANOG (Thermo Fisher Scientific), anti-OCT3/4 (Santa Cruz Biotechnology), anti-SOX1 (Cell Signaling), anti-KI67 (Abcam), anti-γ-tubulin (Abcam), anti-acetylated tubulin (Sigma-Aldrich), anti-ARL13B (Proteintech).

The slides were then washed with PBS containing 0.1% Tween 20, stained with secondary antibodies and DAPI and mounted with the vectashield antifade mounting medium (Vector Laboratories). The slides were viewed with a DeltaVision microscope (GE healthcare). Sum stack of image slices was used for intensity quantification. ImageJ was used to determine the signal intensities of nuclei. Normalized signal intensities were calculated by subtracting background signals from nuclear signals.

Teratoma formation—Human ESCs were injected subcutaneously into 6–8 weeks old female SCID-NOD mice that were obtained from the UT Southwestern Breeding Core or the Jackson Laboratory. For each injection, 1×10^6 cells hESCs were resuspended in 1:1 ratio of cold Matrigel:mTeSR1 media. The cell suspension was kept on ice to maintain Matrigel in liquid phase until injection. Each mouse was injected on both flanks subcutaneously with the same hESC line. At least 3 mice were used for each cell line. Mice were sacrificed at 7–9 weeks after the injection and teratomas were isolated.

Tissue histology and immunohistochemistry—Teratomas were fixed in 10% neutral buffered formalin for 48 h. The fixed tissues were submitted to the Histo Pathology Core at UT Southwestern for processing, embedding, and Hematoxylin and Eosin (H&E) staining. The low and high magnification H&E images of the entire section were captured with a

Leica Aperio CS2 slide scanner. Areas of mature and immature elements were manually marked by a pathologist and quantified using ImageJ.

For immunohistochemistry, unstained slides of sectioned tissues were deparaffinized and epitope/antigen retrieval was performed with 10 mM sodium citrate (pH 6.0). The slides were treated with 0.3% H_2O_2 to block endogenous peroxidase. The slides were then incubated in 3% BSA and stained with the appropriate primary antibodies, including anti-SALL4 (Abcam), anti-GFAP (Abcam), and anti-Glypican-3 (Abcam). After an overnight incubation in primary antibodies, slides were stained with secondary antibodies and DAPI before mounting with the Vectashield mounting medium (Vector Laboratories). The slides were viewed with a DeltaVision microscope.

Quantitative western blotting—Cell pellets were incubated with 1X SDS sample buffer and then lysed by sonication. Lysates were cleared by centrifugation and analyzed by SDS-PAGE followed by Western blotting. The following primary antibodies were used: anti-p53 DO-1 (Santa Cruz Biotechnology) that recognizes epitopes in the region containing residues 11–25, anti-p53 pAB1801 (Santa Cruz Biotechnology) that recognizes epitopes in the region containing residues 32–79, anti-p53 C-terminal antibody (Sigma-Aldrich) that recognizes epitopes in the region containing residues 334–383, anti-GAPDH (Cell Signaling Technology), anti-OCT3/4 (Santa Cruz Biotechnology), anti-SOX2 (Abcam), anti-NANOG (Santa Cruz Biotechnology), anti-Tubulin (Millipore Sigma) and anti-BBS9 (Millipore Sigma). Secondary antibodies used were anti-rabbit or anti-mouse IgG (H + L) (Dylight 680 or 800 conjugates) (Cell Signaling Technology). The membranes were scanned with the Odyssey infrared imaging system (LI-COR Biosciences).

Neural differentiation—Human ESCs were differentiated into neural progenitor cells (NPCs) using the STEMdiff neural system (STEMCELL Technologies). Briefly, 2-3 X 10^6 hESCs suspended in the neural induction medium with the ROCK inhibitor Y27632 were seeded on AggreWell 800 plates (STEMCELL Technologies) for embryoid body (EB) formation. The neural induction medium was changed every day for 5 days. EBs were harvested on day 5 using 37-μm reversible strainers. Collected EBs were replated on fresh Matrigel-coated plates and incubated for 7 days to allow neural rosette (NR) formation. NRs were then selected using STEMdiff NR selection reagent. Selected cells were replated and allowed to grow for another 4-6 days in neural induction medium to form neural progenitor cells (NPCs). NPCs were passaged in STEMdiff neural progenitor medium.

RNA-seq—RNA was extracted from hESCs and NPCs using TRIzol and isopropanol precipitation. Briefly, the cell pellet was incubated with TRIzol and lysed through pipetting. For RNA extraction from teratoma tissues, the frozen tissues were sonicated in TRIzol. After cell and tissue homogenization, chloroform was added to the samples. The samples were vortexed, incubated for 2 min, and centrifuged at 11,000 g for 15 min at 4C to remove cellular debris. The supernatant was transferred to a fresh tube, and isopropanol was added to precipitate the RNA. After centrifugation and washes with 70% ethanol, the RNA was resuspended in nuclease-free water. Purified RNA was analyzed to determine the RNA integrity number (RIN). Samples with RINs greater than 8 were used for library preparation.

For library construction, RNAs were isolated from two different teratomas for each WT or *TP53*$^{-/-}$ cell line and from biological replicates of hESCs and NPCs cell lines. To make libraries for sequencing, TruSeq Stranded mRNA Library Preparation Kit (Illumina) was used to make the libraries for sequencing according to the manufacturer's instructions. After verification of the library quality, 75-bp single-end sequencing was performed on 12 multiplexed libraries pooled together in one flow cell using a NextSeq 500 high output sequencer (Illumina).

Raw FASTQ files were analyzed using FastQC (v0.11.2) (Andrews, 2010) and FastQ Screen (v0.4.4) (Wingett and Andrews, 2018), and reads were quality-trimmed using fastq-mcf (ea-utils/1.1.2–806) (Aronesty, 2013). The trimmed reads were mapped to the hg19 assembly of the human genome (University of California at Santa Cruz, version from iGenomes) using STAR v2.5.3a (Dobin et al., 2013). Duplicated reads were marked using Picard tools (v1.127; https://broadinstitute.github.io/picard/). The RNA counts generated from FeatureCounts (Liao et al., 2014) were TMM normalized (Robinson et al., 2010), and differential expression analysis was performed using edgeR (Huang da et al., 2009). Statistical cutoffs of p value ≤0.05 and $\log_2$CPM ≥0 and were used to identify statistically significant differentially expressed genes (DEGs). Pathway analysis of genes was performed using the gene set enrichment analysis software (GSEA) (Mootha et al., 2003; Subramanian et al., 2005). DEGs heatmaps were clustered by hierarchical clustering using R (http://www.R-project.org) and generated using the Complex Heatmap package (Gu et al., 2016). Tissue specific enrichment analysis (TSEA, http://genetics.wustl.edu/jdlab/tsea/) was performed on the top 200 DEGs between WT and *TP53*$^{-/-}$ teratomas (Wells et al., 2015). Predefined pSI values as provided for the pSI package were used.

Whole genome sequencing—Genomic DNA from cells or teratomas was isolated using the DNeasy Blood & Tissue kit (Qiagen) as per manufacturer's instructions. The DNA was submitted to Beijing Genomics Institute (BGI) for library preparation and next-generation sequencing (NGS). For copy number analysis, the sequencing reads were aligned to the human reference genome (hg19, with Y chromosome removed) using BWA (v 0.7.12) (Li, 2013). Duplicate reads were removed from the alignment using Picard tools (c 2.2.1) (http://broadinstitute.github.io/picard/). HMM copy (v 1.18.0) was used to detect copy number variations (Lai and Shah, 2016). A $\log_2$ ratio of greater than 0.3 was considered a chromosome gain and a $\log_2$ ratio smaller than −0.3 was considered a chromosome loss.

Chromatin immunoprecipitation sequencing (ChIP-seq)—hESCs and NPCs (with 10–15×10^6 cells in each sample) were collected and chemically cross-linked by the addition of 1% formaldehyde for 5 min followed by treatment with 125 mM glycine for 5 min. Cells are then washed twice with PBS and resuspended in the sonication buffer (10 mM Tris HCl pH 7.4, 1 mM EDTA, 0.1% NaDOC, 1% Triton X-100, 0.1% SDS, 0.25% sarkosyl, 1 mM DTT, protease inhibitors from Roche). The cells were sonicated on ice to shear DNA to 300–500 bp. The size of the sheared DNA was confirmed by agarose gel electrophoresis. The whole cell extract was centrifuged for 10 min at 18,000 g at 4°C. The supernatant was transferred to a fresh tube and incubated overnight at 4°C with the p53 antibody (DO-1, Santa Cruz Biotechnology). Samples were then incubated with

pre-washed magnetic Dynabeads (Protein G; Thermo Fisher Scientific-cat#10004D) at 4°C for 2 h. Beads were washed twice with the sonication buffer containing 300 mM NaCl, twice with the sonication buffer containing 500 mM NaCl, twice with the sonication buffer with LiCl (10 mM Tris HCl pH 8.1, 250 mM LiCl, 0.5% NP-40, 0.5% NaDOC, 1 mM EDTA pH 8.0), and twice with the TE buffer (10 mM Tris-HCl, pH 7.5 and 1 mM EDTA pH 8.0). Protein-DNA complexes were eluted from the beads and crosslinking was reversed by overnight incubation in the SDS elution buffer (50 mM Tris-HCl pH 8.1, 1 mM EDTA pH 8.0 and 1% SDS) at 65°C. The immunoprecipitated DNA was treated with RNaseA and proteinase K and recovered using the PCR purification kit (Qiagen). The DNA was then subjected to quality control with Qubit Fluorometer and TapeStation. Libraries from 5–10 ng of ChIP DNA was prepared using the KAPA HTP Library Preparation Kit (Roche) by the Next-Generation Sequencing Core at UT Southwestern. ChIP-seq libraries were sequenced on an Illumina NextSeq 500 using 75 cycle SBS v2 reagents.

Raw FASTQ files were analyzed using FastQC (v0.11.2) (Andrews, 2010) and FastQ_Screen (v0.4.4) (Wingett and Andrews, 2018), and reads were quality-trimmed using fastq-mcf (ea-utils/1.1.2–806) (Aronesty, 2013). The trimmed reads were mapped to the hg19 assembly of the human genome (University of California at Santa Cruz, version from iGenomes) with bowtie2 (version 2.2.3) (Langmead and Salzberg, 2012). The ChIP-seq peaks were called using MACS2 (version 2.0.10) (Zhang et al., 2008), with a q-value threshold of 0.05 and using the random background of ChIP samples as controls. ChIP-seq peaks were annotated using ChIPseeker (Yu et al., 2015) and motif enrichment analysis was done using HOMER (Heinz et al., 2010). Peak occupancy differences were found using intersectBed tool from BEDTools (Quinlan and Hall, 2010).

CRISPR-Cas9 screen—Human GeCKO v2 library was obtained from Addgene (#1000000048) and amplified according to the provided instructions. The amplified GeCKO libraries A and B were combined at 1:1 ratio to make the complete GeCKO library. HEK 293FT cells were transfected with the GeCKO library plasmids and the viral packaging vectors pMD2.G and psPAX2 using Lipofectamine 2000 (Thermo Fisher Scientific). Lentiviral supernatant was harvested at 48 h and 54 h after transfection and concentrated using the lenti-X concentrator (Clontech) at 4°C for 12–36 h. After incubation, virus-containing media were centrifuged at 1,500g for 45 min at 4°C, and viral particles were resuspended in PBS and stored at −80°C until use.

For viral titer determination, H9 WT ESCs were infected with different amounts of lentivirus. At 48 h after transduction, cells were dissociated using Accutase and re-seeded on Matrigel-coated plates with or without 0.5 μg/mL puromycin. After another 48 h, when non-transduced cells were all killed by puromycin, cells were dissociated from wells with or without puromycin and counted to determine the transduction efficiency. The amounts of viruses that generated 30–50% transduction efficiency (MOI = 0.3–1) were used for subsequent CRISPR-Cas9 screen.

Two biological repeats of H9 ESCs were infected with GeCKO v2 lentiviruses at MOI≤1. For 7 days, cells were maintained in mTeSR1-cGMP with puromycin, and a library coverage greater than 500× was ensured during passaging. At day 7 after transduction, puromycin

was withdrawn and cells were cultured for one additional day in mTeSR1-cGMP. At day 8, when cells reached ~80% confluency, cells were collected and resuspended in STEMdiff™ SMADi Neural Induction medium supplemented with the ROCK inhibitor Y27632 and seeded onto Matrigel-coated 6-well plates. Cells were fed daily with STEMdiff™ SMADi neural induction medium and cultured for 7 days. At day 7 of neural induction, the cells were dissociated with Accutase, pooled, and washed with PBS. 6×10^8 cells were fixed with 30 mL BD Phosflow™ Fix Buffer I (BD Biosciences) for 20 min at room temperature. After being washed twice with PBS, cells were resuspended in 25 mL BD Phosflow™ Perm Buffer III (BD Biosciences) and stored at −20°C.

About 3×10^8 cells stored in BD Phosflow™ Perm Buffer III were washed twice with 1% PBSA buffer (PBS containing 1% BSA) and then incubated with rabbit anti-SOX1 antibody (Cell Signaling Technology, #4194) at 1:150 dilution for 1 h at room temperature. Cells were washed twice with the PBSA buffer and incubated with the Alexa Fluor® 488 Donkey Anti-rabbit IgG (H + L) Antibody (Thermo Fisher Scientific) at 1:500 dilution for 30 min at room temperature. After being washed twice with the PBSA buffer, cells were resuspended in 8 mL PBSA buffer. Cells were filtered using the 40-μm cell strainer and sorted using BD FACSAria II SORP or BD FACSAria Fusion sorters. The 1% of cell population with the lowest SOX1 signal was collected. Unsorted cells were also similarly treated and collected.

Genomic DNA was extracted from fixed cells as described (Golden et al., 2017) with minor modifications. The sorted cells were resuspended in 600 μL STE lysis buffer (11 mM EDTA pH 8.0, 10 mM Tris-HCl pH 8.0, 100 mM NaCl, 250 μg/mL proteinase K, 0.25% SDS). 6×10^6 unsorted cells were resuspended in 1 mL STE lysis buffer. Cell lysis was performed by an overnight incubation at 55°C with occasional vortexing. RNase A (1 mg) was then added to each tube and the samples were incubated at 37°C for 1 h while shaking. gDNA extraction was performed with an equal volume of buffer-saturated phenol (pH 7.9), followed by phenol:chloroform: isoamyl alcohol (25:24:1), followed by chloroform. The aqueous phase after chloroform extraction was separated into 300 μL aliquots in 1.5-mL microtubes. 7.5 μg of Glycoblue (Thermo Fisher Scientific) and 900 μL ethanol were added to each tube and the samples were incubated overnight at −80°C. gDNA was precipitated by centrifugation at 18,000 g for 15 min at 4°C, washed with 1 mL 75% ethanol, air dried for 10 min, and resuspended and incubated in 50 ul buffer AE (10 mM Tris-Cl, 0.5 mM EDTA, pH 9.0) at 37°C for about 10 h. The DNA concentration was measured with the Qubit dsDNA BR assay kit (Thermo Fisher Scientific).

Two rounds of PCR were performed for each gDNA sample to amplify gRNA cassettes with Illumina sequencing adapters and indexes (Sanjana et al., 2014; Shalem et al., 2014). In the first round of PCR (PCR-I), 20 cycles of amplification were performed using Herculase II DNA polymerase (Agilent). For sorted cells, all gDNA from a given sample was distributed into three 50 μL reactions. For unsorted cells, 2 μg of gDNA was used in each 50 μL PCR reaction and a total of 90 reactions were performed to maintain 300× coverage of the library. After PCR-I, all PCR product from a given sample was pooled and mix thoroughly. In the second round of PCR (PCR-II), 2.5 μL of PCR-I product was used as template in each 50 μL reaction. 30 reactions and 6 reactions were performed for unsorted and sorted cells, respectively, to maintain library coverage. The PCR cycle number was

optimized (ranging from 10–14 cycles) for each sample to produce similar DNA yield. PCR-II product from a given sample was pooled and DNA was purified with AMPure XP beads (Beckman Coulter) according to the manufacturer's instructions. After being eluted with 40 μL nuclease-free water, all DNA libraries were checked with Agilent BioAnalyzer High Sensitivity DNA Analysis Kit (Agilent). DNA concentration was measured both by Qubit dsDNA HS assay kit (Thermo Fisher Scientific) and by qPCR using a KAPA Library Quantification Kit (Roche) for Illumina platforms. All samples were pooled and sequenced on Illumina NextSeq 500 sequencer with read configuration as 75 bp, single end and about 20-30 million reads per sample.

The FASTQ files were subjected to quality check using FastQC (v0.11.2) and FastQ_Screen (v0.4.4) (Wingett and Andrews, 2018), and adapters were trimmed using an in-house script. The reference sgRNA library sequences for human GeCKO v2.0 (A and B) were downloaded from Addgene (https://www.addgene.org/pooled-library/). The trimmed FASTQ files were mapped to the reference sgRNA library with mismatch option as 0 using MAGeCK (Li et al., 2014). Read counts for each sgRNA were generated and median normalization was performed to adjust for library sizes. Positively and negatively selected sgRNA and genes were identified with MAGeCK using the default parameters.

QUANTIFICATION AND STATISTICAL ANALYSIS

Prism 8 and Prism 9 were used for all statistical analysis. Details on number of repeats (n) can be found in figure legends. Values in graphs represent mean ± SD. Statistical significance was determined using unpaired student t test in Prism and interpreted as significant if $p < 0.05$.

Supplementary Material

Refer to Web version on PubMed Central for supplementary material.

ACKNOWLEDGMENTS

We thank Eunhee Choi and Sean Goetsch for technical assistance with the teratoma assay, and Sergii Kyrychenko and Jay Schneider for assistance with CRISPR-Cas9 gene targeting in hESCs. We also thank members of the McDermott Sequencing Core at UT Southwestern for providing technical assistance with next-generation sequencing (NGS) experiments. This study was supported by grants from the Howard Hughes Medical Institute, the National Institutes of Health (1R01GM124096), Cancer Prevention and Research Institute of Texas (RP160667-P2), and the Welch Foundation (I-1441).

REFERENCES

Abbas T, and Dutta A (2009). p21 in cancer: intricate networks and multiple activities. Nat. Rev. Cancer 9, 400–414. [PubMed: 19440234]

Amin MB, Gress DM, Meyer Vega LR, and Edge SB (2017). AJCC Cancer Staging Manual, 8th edn (Springer).

Andrews S (2010). FastQC: A Quality Control Tool for High Throughput Sequence Data. http://www.bioinformatics.babraham.ac.uk/projects/fastqc.

Aoubala M, Murray-Zmijewski F, Khoury MP, Fernandes K, Perrier S, Bernard H, Prats AC, Lane DP, and Bourdon JC (2011). p53 directly transactivates Delta133p53alpha, regulating cell fate outcome in response to DNA damage. Cell Death Differ 18, 248–258. [PubMed: 20689555]

Armstrong JF, Kaufman MH, Harrison DJ, and Clarke AR (1995). High-frequency developmental abnormalities in p53-deficient mice. Curr. Biol 5, 931–936. [PubMed: 7583151]

Aronesty E (2013). Comparison of sequencing utility programs. Open Bioinf. J 7, 1–8.

Bangs F, and Anderson KV (2017). Primary cilia and mammalian hedgehog signaling. Cold Spring Harb. Perspect. Biol 9, a028175. [PubMed: 27881449]

Ben-David U, and Amon A (2020). Context is everything: aneuploidy in cancer. Nat. Rev. Genet 21, 44–62. [PubMed: 31548659]

Briscoe J, and Therond PP (2013). The mechanisms of Hedgehog signalling and its roles in development and disease. Nat. Rev. Mol. Cell Biol 14, 416–429. [PubMed: 23719536]

Bunz F, Fauth C, Speicher MR, Dutriaux A, Sedivy JM, Kinzler KW, Vogelstein B, and Lengauer C (2002). Targeted inactivation of p53 in human cells does not result in aneuploidy. Cancer Res. 62, 1129–1133. [PubMed: 11861393]

Chambers SM, Fasano CA, Papapetrou EP, Tomishima M, Sadelain M, and Studer L (2009). Highly efficient neural conversion of human ES and iPS cells by dual inhibition of SMAD signaling. Nat. Biotechnol 27, 275–280. [PubMed: 19252484]

Chung JH, Larsen AR, Chen E, and Bunz F (2014). A PTCH1 homolog transcriptionally activated by p53 suppresses Hedgehog signaling. J. Biol. Chem 289, 33020–33031. [PubMed: 25296753]

Cordenonsi M, Dupont S, Maretto S, Insinga A, Imbriano C, and Piccolo S (2003). Links between tumor suppressors: p53 is required for TGF-beta gene responses by cooperating with Smads. Cell 113, 301–314. [PubMed: 12732139]

Courtois S, Verhaegh G, North S, Luciani MG, Lassus P, Hibner U, Oren M, and Hainaut P (2002). DeltaN-p53, a natural isoform of p53 lacking the first transactivation domain, counteracts growth suppression by wild-type p53. Oncogene 21, 6722–6728. [PubMed: 12360399]

Deglincerti A, Etoc F, Ozair MZ, and Brivanlou AH (2016). Self-organization of spatial patterning in human embryonic stem cells. Curr. Top. Dev. Biol 116, 99–113. [PubMed: 26970615]

Dobin A, Davis CA, Schlesinger F, Drenkow J, Zaleski C, Jha S, Batut P, Chaisson M, and Gingeras TR (2013). STAR: ultrafast universal RNA-seq aligner. Bioinformatics 29, 15–21. [PubMed: 23104886]

Donehower LA, Harvey M, Slagle BL, McArthur MJ, Montgomery CA Jr., Butel JS, and Bradley A (1992). Mice deficient for p53 are developmentally normal but susceptible to spontaneous tumours. Nature 356, 215–221. [PubMed: 1552940]

Drost J, van Jaarsveld RH, Ponsioen B, Zimberlin C, van Boxtel R, Buijs A, Sachs N, Overmeer RM, Offerhaus GJ, Begthel H, et al. (2015). Sequential cancer mutations in cultured human intestinal stem cells. Nature 521, 43–47. [PubMed: 25924068]

Elkabetz Y, Panagiotakos G, Al Shamy G, Socci ND, Tabar V, and Studer L (2008). Human ES cell-derived neural rosettes reveal a functionally distinct early neural stem cell stage. Genes Dev. 22, 152–165. [PubMed: 18198334]

Ferrante MI, Zullo A, Barra A, Bimonte S, Messaddeq N, Studer M, Dolle P, and Franco B (2006). Oral-facial-digital type I protein is required for primary cilia formation and left-right axis specification. Nat. Genet 38, 112–117. [PubMed: 16311594]

Goetz SC, and Anderson KV (2010). The primary cilium: a signalling centre during vertebrate development. Nat. Rev. Genet 11, 331–344. [PubMed: 20395968]

Golden RJ, Chen B, Li T, Braun J, Manjunath H, Chen X, Wu J, Schmid V, Chang TC, Kopp F, et al. (2017). An Argonaute phosphorylation cycle promotes microRNA-mediated silencing. Nature 542, 197–202. [PubMed: 28114302]

Gu Z, Eils R, and Schlesner M (2016). Complex heatmaps reveal patterns and correlations in multidimensional genomic data. Bioinformatics 32, 2847–2849. [PubMed: 27207943]

Han YG, Kim HJ, Dlugosz AA, Ellison DW, Gilbertson RJ, and Alvarez-Buylla A (2009). Dual and opposing roles of primary cilia in medulloblastoma development. Nat. Med 15, 1062–1065. [PubMed: 19701203]

He Q, Wang G, Wakade S, Dasgupta S, Dinkins M, Kong JN, Spas-sieva SD, and Bieberich E (2014). Primary cilia in stem cells and neural progenitors are regulated by neutral sphingomyelinase 2 and ceramide. Mol. Biol. Cell 25, 1715–1729. [PubMed: 24694597]

Heinz S, Benner C, Spann N, Bertolino E, Lin YC, Laslo P, Cheng JX, Murre C, Singh H, and Glass CK (2010). Simple combinations of lineage-determining transcription factors prime cis-regulatory elements required for macrophage and B cell identities. Mol. Cell 38, 576–589. [PubMed: 20513432]

Hong H, Takahashi K, Ichisaka T, Aoi T, Kanagawa O, Nakagawa M, Okita K, and Yamanaka S (2009). Suppression of induced pluripotent stem cell generation by the p53-p21 pathway. Nature 460, 1132–1135. [PubMed: 19668191]

Huang da W, Sherman BT, and Lempicki RA (2009). Systematic and integrative analysis of large gene lists using DAVID bioinformatics resources. Nat. Protoc 4, 44–57. [PubMed: 19131956]

Huangfu D, and Anderson KV (2005). Cilia and Hedgehog responsiveness in the mouse. Proc. Natl. Acad. Sci. U. S. A 102, 11325–11330. [PubMed: 16061793]

Hunkapiller J, Singla V, Seol A, and Reiter JF (2011). The ciliogenic protein Oral-Facial-Digital 1 regulates the neuronal differentiation of embryonic stem cells. Stem Cells Dev 20, 831–841. [PubMed: 20873986]

Kastenhuber ER, and Lowe SW (2017). Putting p53 in context. Cell 170, 1062–1078. [PubMed: 28886379]

Kawamura T, Suzuki J, Wang YV, Menendez S, Morera LB, Raya A, Wahl GM, and Izpisua Belmonte JC (2009). Linking the p53 tumour suppressor pathway to somatic cell reprogramming. Nature 460, 1140–1144. [PubMed: 19668186]

Kiprilov EN, Awan A, Desprat R, Velho M, Clement CA, Byskov AG, Andersen CY, Satir P, Bouhassira EE, Christensen ST, et al. (2008). Human embryonic stem cells in culture possess primary cilia with hedgehog signaling machinery. J. Cell Biol 180, 897–904. [PubMed: 18332216]

Lai DHG, and Shah S (2016). HMMcopy: Copy Number Prediction with Correction for GC and Mappability Bias for HTS Data.

Langmead B, and Salzberg SL (2012). Fast gapped-read alignment with Bowtie 2. Nat. Methods 9, 357–359. [PubMed: 22388286]

Lee DF, Su J, Kim HS, Chang B, Papatsenko D, Zhao R, Yuan Y, Gingold J, Xia W, Darr H, et al. (2015). Modeling familial cancer with induced pluripotent stem cells. Cell 161, 240–254. [PubMed: 25860607]

Li H (2013). Aligning Sequence Reads, Clone Sequences and Assembly Contigs with BWA-MEM (arXiv), arXiv:1303.3997v2.

Li W, Xu H, Xiao T, Cong L, Love MI, Zhang F, Irizarry RA, Liu JS, Brown M, and Liu XS (2014). MAGeCK enables robust identification of essential genes from genome-scale CRISPR/Cas9 knockout screens. Genome Biol. 15, 554. [PubMed: 25476604]

Liao Y, Smyth GK, and Shi W (2014). featureCounts: an efficient general purpose program for assigning sequence reads to genomic features. Bioinformatics 30, 923–930. [PubMed: 24227677]

Lin T, Chao C, Saito S, Mazur SJ, Murphy ME, Appella E, and Xu Y (2005). p53 induces differentiation of mouse embryonic stem cells by suppressing Nanog expression. Nat. Cell Biol 7, 165–171. [PubMed: 15619621]

Liu A, Wang B, and Niswander LA (2005). Mouse intraflagellar transport proteins regulate both the activator and repressor functions of Gli transcription factors. Development 132, 3103–3111. [PubMed: 15930098]

Liu H, Kiseleva AA, and Golemis EA (2018). Ciliary signalling in cancer. Nat. Rev. Cancer 18, 511–524. [PubMed: 29802351]

Malkin D, Li FP, Strong LC, Fraumeni JF Jr., Nelson CE, Kim DH, Kassel J, Gryka MA, Bischoff FZ, Tainsky MA, et al. (1990). Germ line p53 mutations in a familial syndrome of breast cancer, sarcomas, and other neoplasms. Science 250, 1233–1238. [PubMed: 1978757]

Marin Navarro A, Pronk RJ, van der Geest AT, Oliynyk G, Nordgren A, Arsenian-Henriksson M, Falk A, and Wilhelm M (2020). p53 controls genomic stability and temporal differentiation of human neural stem cells and affects neural organization in human brain organoids. Cell Death Dis 11, 52. [PubMed: 31974372]

Marion RM, Strati K, Li H, Murga M, Blanco R, Ortega S, Fernandez-Capetillo O, Serrano M, and Blasco MA (2009). A p53-mediated DNA damage response limits reprogramming to ensure iPS cell genomic integrity. Nature 460, 1149–1153. [PubMed: 19668189]

May SR, Ashique AM, Karlen M, Wang B, Shen Y, Zarbalis K, Reiter J, Ericson J, and Peterson AS (2005). Loss of the retrograde motor for IFT disrupts localization of Smo to cilia and prevents the expression of both activator and repressor functions of Gli. Dev. Biol 287, 378–389. [PubMed: 16229832]

McDonald D, Wu Y, Dailamy A, Tat J, Parekh U, Zhao D, Hu M, Tipps A, Zhang K, and Mali P (2020). Defining the teratoma as a model for multilineage human development. Cell 183, 1402–1419.e1418. [PubMed: 33152263]

Merkle FT, Ghosh S, Kamitaki N, Mitchell J, Avior Y, Mello C, Kashin S, Mekhoubad S, Ilic D, Charlton M, et al. (2017). Human pluripotent stem cells recurrently acquire and expand dominant negative P53 mutations. Nature 545, 229–233. [PubMed: 28445466]

Molchadsky A, Rivlin N, Brosh R, Rotter V, and Sarig R (2010). p53 is balancing development, differentiation and de-differentiation to assure cancer prevention. Carcinogenesis 31, 1501–1508. [PubMed: 20504879]

Mootha VK, Lindgren CM, Eriksson KF, Subramanian A, Sihag S, Lehar J, Puigserver P, Carlsson E, Ridderstrale M, Laurila E, et al. (2003). PGC-1α-responsive genes involved in oxidative phosphorylation are coordinately downregulated in human diabetes. Nat. Genet 34, 267–273. [PubMed: 12808457]

Pfister K, Pipka JL, Chiang C, Liu Y, Clark RA, Keller R, Skoglund P, Guertin MJ, Hall IM, and Stukenberg PT (2018). Identification of drivers of aneuploidy in breast tumors. Cell Rep 23, 2758–2769. [PubMed: 29847804]

Picariello T, Brown JM, Hou Y, Swank G, Cochran DA, King OD, Lechtreck K, Pazour GJ, and Witman GB (2019). A global analysis of IFT-A function reveals specialization for transport of membrane-associated proteins into cilia. J. Cell Sci 132, jcs220749. [PubMed: 30659111]

Quinlan AR, and Hall IM (2010). BEDTools: a flexible suite of utilities for comparing genomic features. Bioinformatics 26, 841–842. [PubMed: 20110278]

Ran FA, Hsu PD, Wright J, Agarwala V, Scott DA, and Zhang F (2013). Genome engineering using the CRISPR-Cas9 system. Nat. Protoc 8, 2281–2308. [PubMed: 24157548]

Robinson MD, McCarthy DJ, and Smyth GK (2010). edgeR: a Bioconductor package for differential expression analysis of digital gene expression data. Bioinformatics 26, 139–140. [PubMed: 19910308]

Sanjana NE, Shalem O, and Zhang F (2014). Improved vectors and genome-wide libraries for CRISPR screening. Nat. Methods 11, 783–784. [PubMed: 25075903]

Schmidts M, Frank V, Eisenberger T, Al Turki S, Bizet AA, Antony D, Rix S, Decker C, Bachmann N, Bald M, et al. (2013). Combined NGS approaches identify mutations in the intraflagellar transport gene IFT140 in skeletal ciliopathies with early progressive kidney Disease. Hum. Mutat 34, 714–724. [PubMed: 23418020]

Shalem O, Sanjana NE, Hartenian E, Shi X, Scott DA, Mikkelsen TS, Heckl D, Ebert BL, Root DE, Doench JG, et al. (2014). Genome-scale CRISPR-Cas9 knockout screening in human cells. Science 343, 84–87. [PubMed: 24336571]

Shen H, Shih J, Hollern DP, Wang L, Bowlby R, Tickoo SK, Thorsson V, Mungall AJ, Newton Y, Hegde AM, et al. (2018). Integrated molecular characterization of testicular germ cell tumors. Cell Rep 23, 3392–3406. [PubMed: 29898407]

Solter D (2006). From teratocarcinomas to embryonic stem cells and beyond: a history of embryonic stem cell research. Nat. Rev. Genet 7, 319–327. [PubMed: 16534514]

Song H, Chung SK, and Xu Y (2010). Modeling disease in human ESCs using an efficient BAC-based homologous recombination system. Cell Stem Cell 6, 80–89. [PubMed: 20074536]

Soto M, Raaijmakers JA, Bakker B, Spierings DCJ, Lansdorp PM, Foijer F, and Medema RH (2017). p53 prohibits propagation of chromosome segregation errors that produce structural aneuploidies. Cell Rep 19, 2423–2431. [PubMed: 28636931]

Stamataki D, Ulloa F, Tsoni SV, Mynett A, and Briscoe J (2005). A gradient of Gli activity mediates graded Sonic Hedgehog signaling in the neural tube. Genes Dev. 19, 626–641. [PubMed: 15741323]

Stiewe T (2007). The p53 family in differentiation and tumorigenesis. Nat. Rev. Cancer 7, 165–168. [PubMed: 17332760]

Subramanian A, Tamayo P, Mootha VK, Mukherjee S, Ebert BL, Gillette MA, Paulovich A, Pomeroy SL, Golub TR, Lander ES, et al. (2005). Gene set enrichment analysis: a knowledge-based approach for interpreting genome-wide expression profiles. Proc. Natl. Acad. Sci. U. S. A 102, 15545–15550. [PubMed: 16199517]

Wang Q, Zou Y, Nowotschin S, Kim SY, Li QV, Soh CL, Su J, Zhang C, Shu W, Xi Q, et al. (2017). The p53 family coordinates wnt and nodal inputs in mesendodermal differentiation of embryonic stem cells. Cell Stem Cell 20, 70–86. [PubMed: 27889317]

Wei Q, Zhang Y, Li Y, Zhang Q, Ling K, and Hu J (2012). The BBSome controls IFT assembly and turnaround in cilia. Nat. Cell Biol 14, 950–957. [PubMed: 22922713]

Wells A, Kopp N, Xu X, O'Brien DR, Yang W, Nehorai A, Adair-Kirk TL, Kopan R, and Dougherty JD (2015). The anatomical distribution of genetic associations. Nucleic Acids Res. 43, 10804–10820. [PubMed: 26586807]

Wingett SW, and Andrews S (2018). FastQ screen: a tool for multi-genome mapping and quality control. F1000Res 7, 1338. [PubMed: 30254741]

Yu G, Wang LG, and He QY (2015). ChIPseeker: an R/Bioconductor package for ChIP peak annotation, comparison and visualization. Bioinformatics 31, 2382–2383. [PubMed: 25765347]

Zaghloul NA, and Katsanis N (2009). Mechanistic insights into Bardet-Biedl syndrome, a model ciliopathy. J. Clin. Invest 119, 428–437. [PubMed: 19252258]

Zhang M, Cheng L, Jia Y, Liu G, Li C, Song S, Bradley A, and Huang Y (2016). Aneuploid embryonic stem cells exhibit impaired differentiation and increased neoplastic potential. EMBO J. 35, 2285–2300. [PubMed: 27558554]

Zhang Y, Liu T, Meyer CA, Eeckhoute J, Johnson DS, Bernstein BE, Nusbaum C, Myers RM, Brown M, Li W, et al. (2008). Model-based analysis of ChIP-seq (MACS). Genome Biol. 9, R137. [PubMed: 18798982]

Zhao Z, Zuber J, Diaz-Flores E, Lintault L, Kogan SC, Shannon K, and Lowe SW (2010). p53 loss promotes acute myeloid leukemia by enabling aberrant self-renewal. Genes Dev. 24, 1389–1402. [PubMed: 20595231]

Ziller MJ, Edri R, Yaffe Y, Donaghey J, Pop R, Mallard W, Issner R, Gifford CA, Goren A, Xing J, et al. (2015). Dissecting neural differentiation regulatory networks through epigenetic footprinting. Nature 518, 355–359. [PubMed: 25533951]

Highlights

- *TP53*$^{-/-}$ hESCs form poorly differentiated, immature teratomas in mice
- TP53 is required for hESC differentiation into neural progenitor cells (NPCs)
- Ciliogenesis and Shh signaling organize neural rosettes during NPC differentiation
- TP53 enhances *BBS9* transcription to promote ciliogenesis and NPC differentiation

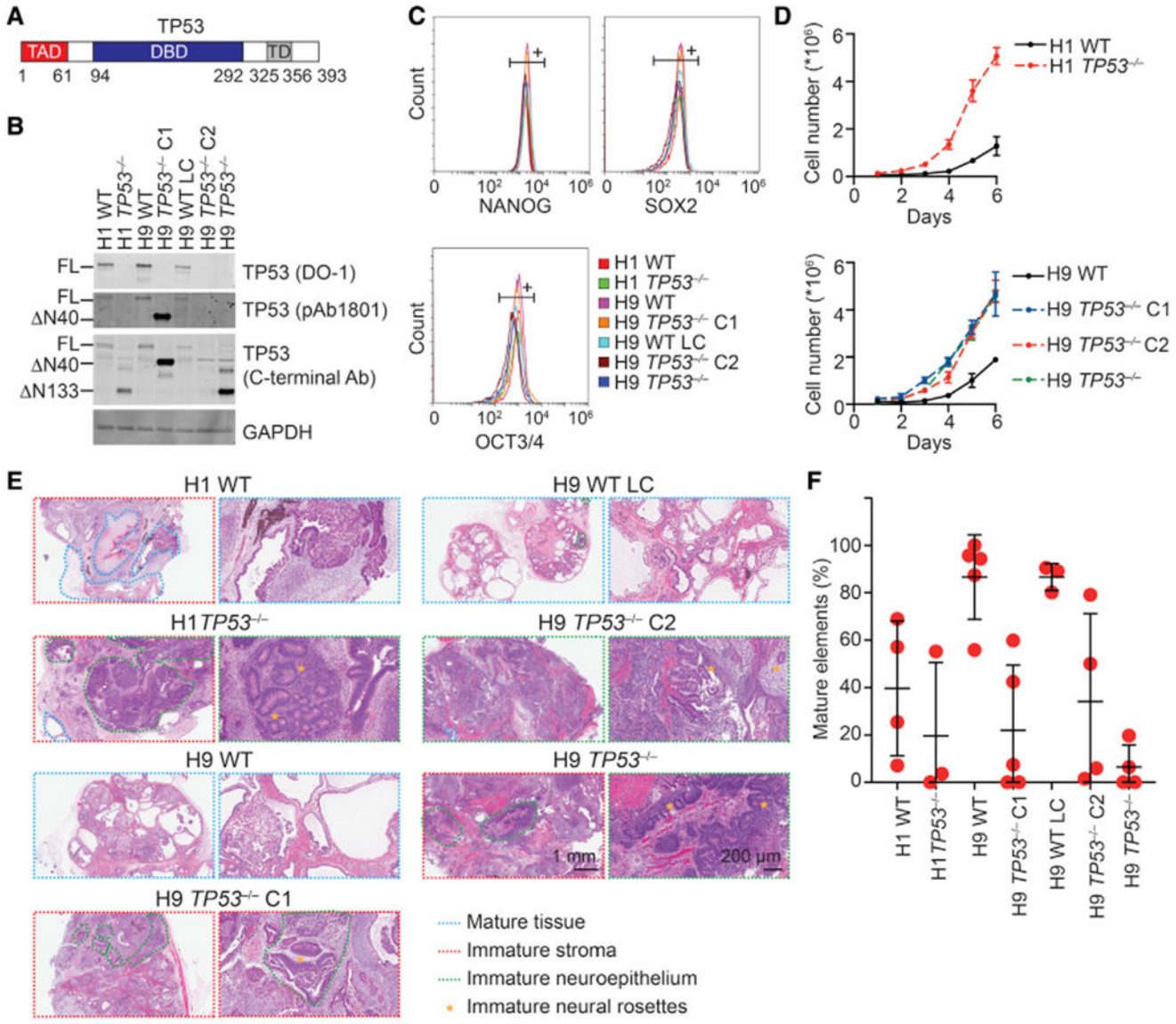

Figure 1. *TP53*$^{-/-}$ hESCs form immature teratomas

(A) Schematic representation of the domains of TP53.

(B) Western blots of total cell lysates of *TP53*$^{-/-}$ hESC clones and pools. The DO-1 antibody detects full-length (FL) TP53. pAb1801 and the TP53 C-terminal antibody detect the N-terminal truncation of TP53 (ΔN40 and ΔN133).

(C) Flow cytometry analysis of wild-type (WT) and *TP53*$^{-/-}$ hESCs stained with pluripotency markers.

(D) Cell proliferation assays of WT and *TP53*$^{-/-}$ hESCs. Mean ± SD; n = 3 independent experiments.

(E) Hematoxylin and eosin (H&E) staining of WT and *TP53*$^{-/-}$ teratoma sections. Mature elements, immature stroma, and immature neuroepithelium are marked by dashed lines of the indicated color. Immature neural rosettes (NRs) are marked by stars.

(F) Quantification of the percentages of mature and immature elements in WT and *TP53*$^{-/-}$ teratoma sections. Mean ± SD; n = 3–5.

DBD, DNA binding domain; TAD, transactivation domain; TD, tetramerization domain.

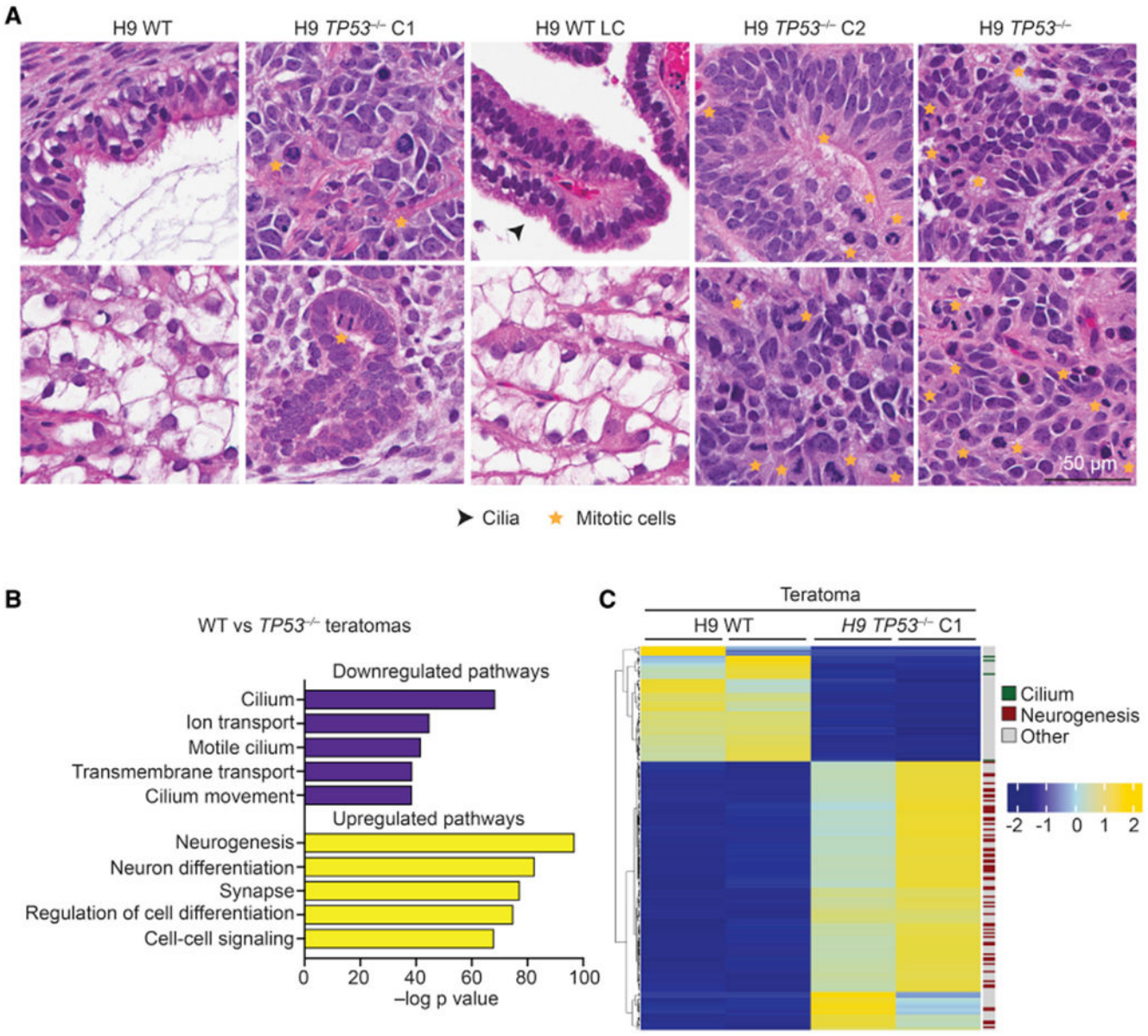

Figure 2. *TP53*$^{-/-}$ hESCs form immature teratomas with deficient neurogenesis and ciliogenesis

(A) H&E staining of WT and *TP53*$^{-/-}$ teratoma sections at high magnification. Arrowheads indicate cilia. Stars indicate mitotic cells.

(B) Gene set enrichment analysis (GSEA) of the differentially expressed genes (DEGs) between WT and *TP53*$^{-/-}$ teratomas.

(C) Heatmap of top 200 DEGs identified by RNA-seq analysis of WT and *TP53*$^{-/-}$ teratomas. DEGs involved in the cilium and neurogenesis pathways are indicated.

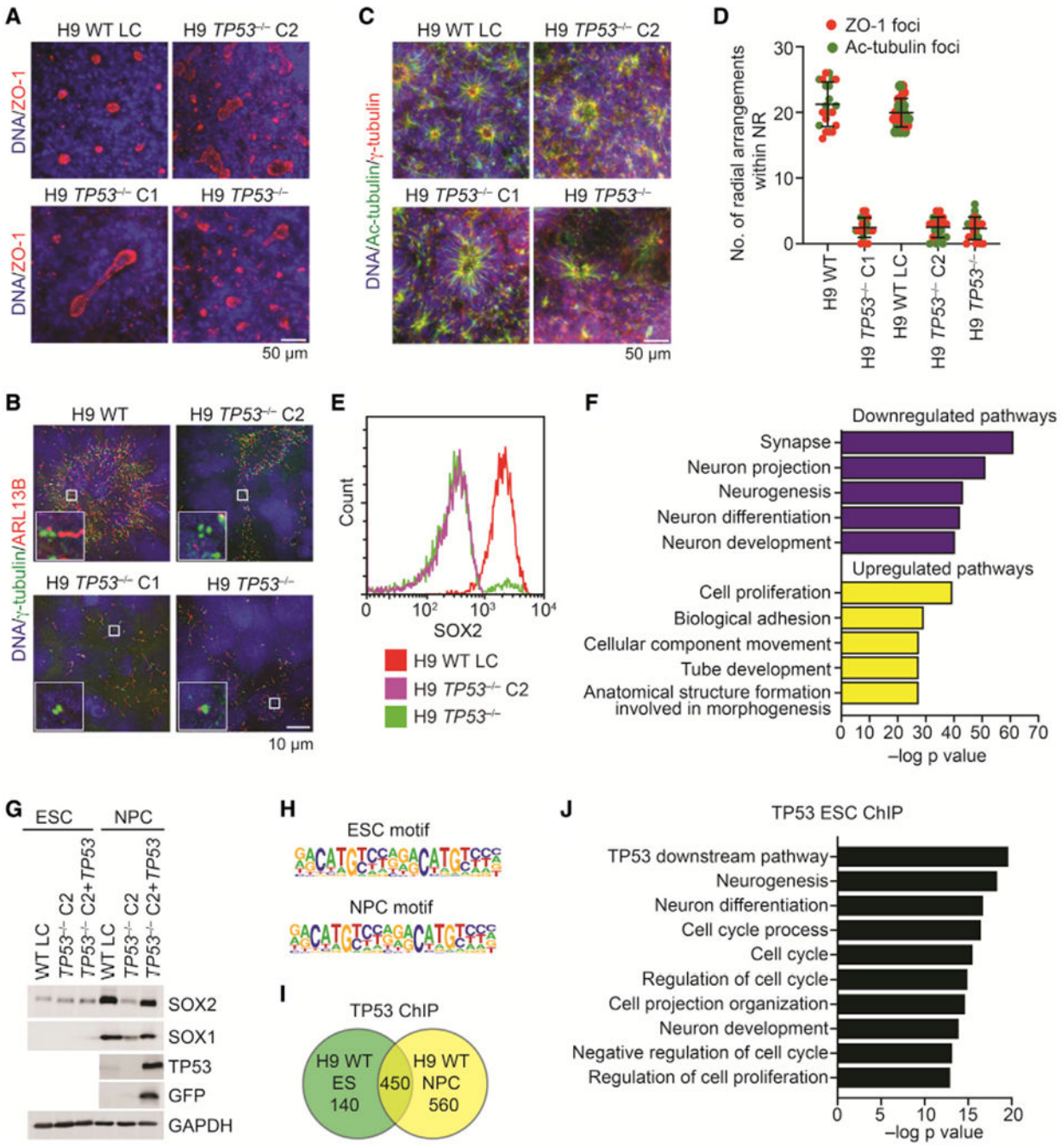

Figure 3. *TP53*$^{-/-}$ hESCs are deficient in differentiation into neural progenitor cells (NPCs) *in vitro*

(A) Immunofluorescence (IF) images of WT and *TP53*$^{-/-}$ NRs at day 11 stained with DAPI for DNA (blue) and the ZO-1 antibody (red).

(B) IF images of WT and *TP53*$^{-/-}$ NRs at day 11 stained with DAPI for DNA (blue) and antibodies against the cilium protein ARL13B (red) and γ-tubulin (green).

(C) IF images of WT and *TP53*$^{-/-}$ NRs at day 11 stained with DAPI for DNA (blue) and antibodies against acetylated tubulin (Ac-tubulin; green) and γ-tubulin (red).

(D) Quantification of the number of radial arrangements (as defined by ZO-1 and Ac-tubulin foci) within each WT or *TP53*$^{-/-}$ NR. Each dot represents one NR. Mean ± SD; n = 10.

(E) Flow cytometry analysis of SOX2 expression in WT and *TP53*$^{-/-}$ NPCs.

(F) GSEA of the 589 common DEGs between WT and *TP53*$^{-/-}$ NPCs.

(G) Western blots of total lysates of WT and *TP53*$^{-/-}$ ESCs and NPCs and *TP53*$^{-/-}$ cells expressing an exogenous *TP53* transgene.

(H) *De novo* motif analysis of TP53 ChIP-seq peaks in ESCs and NPCs.

(I) Venn diagram showing the number and overlap of TP53 ChIP-seq peaks in WT ESCs and NPCs.

(J) GSEA of genes occupied by TP53 in ESCs.

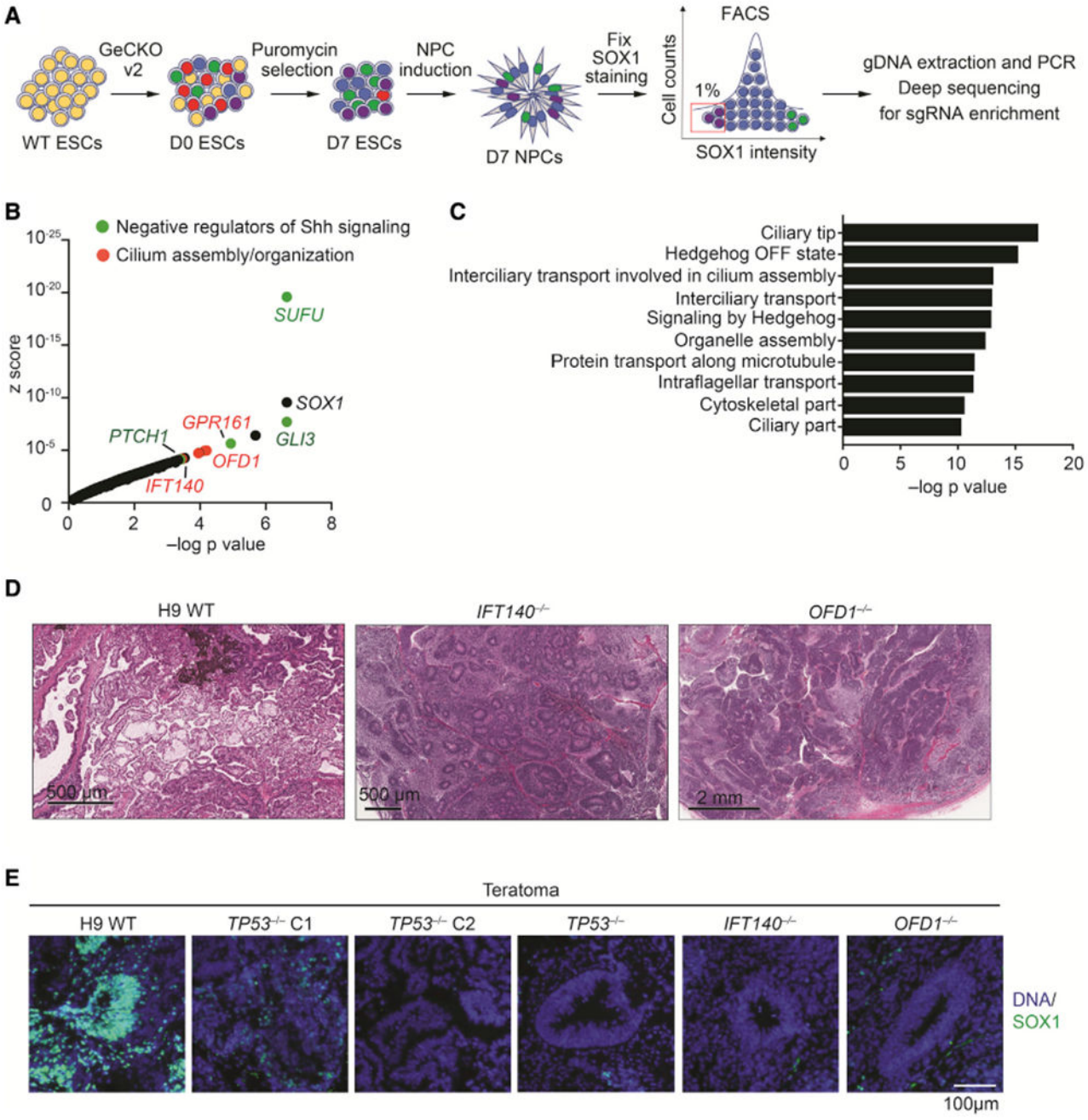

Figure 4. Genome-wide CRISPR screen identifies requirement for ciliogenesis and downregulation of sonic hedgehog (Shh) signaling during NPC differentiation

(A) Flowchart of the CRISPR-Cas9 screen.

(B) Graphical display of CRISPR-Cas9 screen hits ranked by the *Z* score. Top 20 hits with known functions in Shh signaling and ciliogenesis are depicted in green and red dots, respectively.

(C) GSEA of top 500 hits in the CRISPR screen.

(D) H&E staining of WT, *IFT140*$^{-/-}$, and *OFD1*$^{-/-}$ teratoma sections at high magnification. Four teratomas in each group were analyzed with representative images shown.

(E) Immunohistochemistry (IHC) staining of the indicated teratoma sections with DAPI for DNA and the anti-SOX1 antibody.

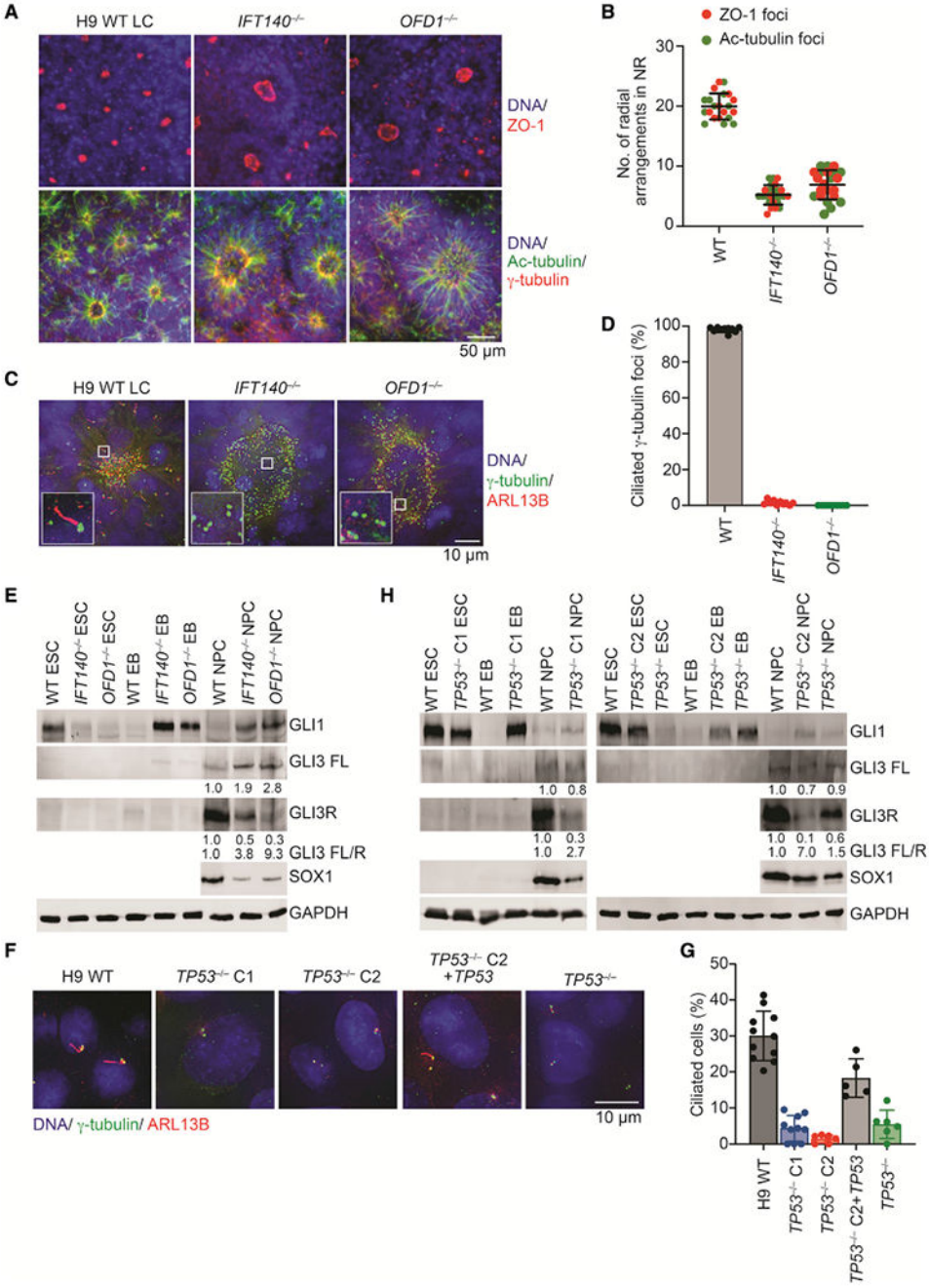

Figure 5. *IFT140*$^{-/-}$, *OFD1*$^{-/-}$, and *TP53*$^{-/-}$ hESCs exhibit deficient ciliogenesis, unrestrained Shh signaling, and defective NPC differentiation

(A) IF images of WT, *IFT140*$^{-/-}$ and *OFD1*$^{-/-}$ NRs stained with DAPI for DNA and the indicated antibodies. Top and bottom panels show different NRs of each cell line.

(B) Quantification of the number of radial arrangements (as defined by ZO-1 and Ac-tubulin foci) within each WT or the indicated mutant NR. Each dot represents one NR. Mean ± SD; n = 10 for both ZO-1 and Ac-tubulin.

(C) IF images of WT, *IFT140*$^{-/-}$, and *OFD1*$^{-/-}$ NRs stained with DAPI for DNA (blue) and antibodies against ARL13B (red) and γ-tubulin (green).

(D) Quantification of the percentage of ciliated γ-tubulin foci in each NR. Mean ± SD; n = 10.

(E) Western blots of lysates of WT, *IFT140*$^{-/-}$, and *OFD1*$^{-/-}$ H9 ESCs, EBs, and NPCs with the indicated antibodies. The relative intensities of GLI3 FL and GLI3R and their ratios are indicated.

(F) IF images of WT ESCs, *TP53*$^{-/-}$ ESCs, and *TP53*$^{-/-}$ ESCs re-expressing the *TP53* transgene stained with DAPI for DNA (blue) and antibodies against ARL13B (red) and γ-tubulin (green).

(G) Quantification of the percentage of ciliated cells in (F). Each dot represents one field of view. Mean ± SD; n = 11 (total 695 cells) for WT; n = 10 (total 237 cells) for *TP53*$^{-/-}$ C1; n = 6 (total 268 cells) for *TP53*$^{-/-}$ C2; n = 5 (total 183) for *TP53*$^{-/-}$ C2 re-expressing *TP53;* n = 6 (total 290) for *TP53*$^{-/-}$.

(H) Western blots of lysates of WT and *TP53*$^{-/-}$ ESCs, EBs, and NPCs with the indicated antibodies. The relative intensities of GLI3 FL and GLI3R and their ratios are indicated.

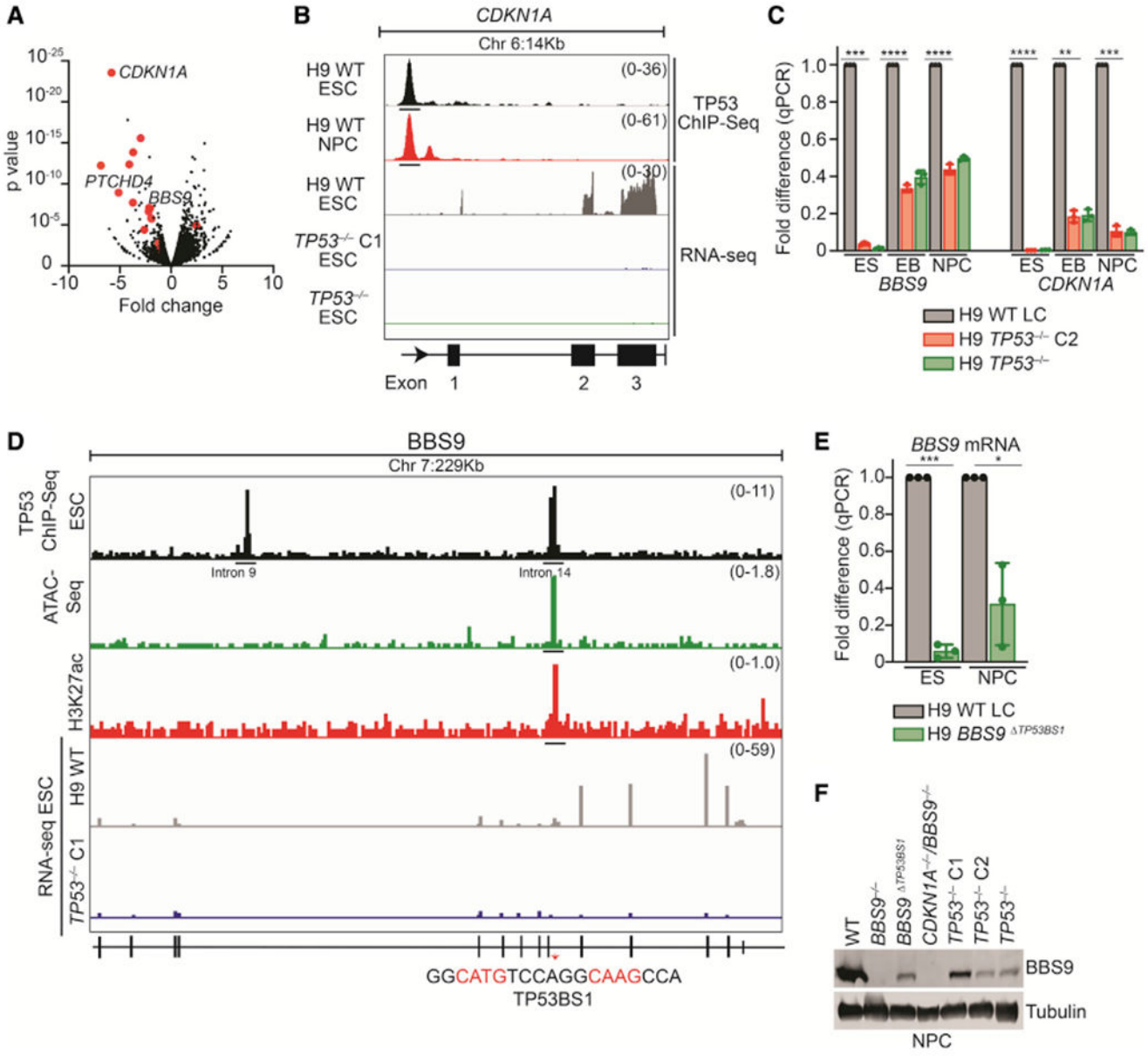

Figure 6. *BBS9* is a TP53 target gene

(A) Volcano plot of RNA-seq data of WT and *TP53*$^{-/-}$ ESCs showing the $\log_2$ fold change and p value of individual genes. DEGs with TP53 ChIP-seq peaks in their vicinity are shown as red dots.

(B) TP53 ChIP-seq and RNA-seq tracks from the Integrative Genomics Viewer in the *CDKN1A* gene in WT hESCs and NPCs and in *TP53*$^{-/-}$ hESCs. The TP53 ChIP-seq peaks in the *CDKN1A* promoter are underlined.

(C) qPCR analysis of the mRNA levels of *BBS9* and *CDKN1A* in WT and *TP53*$^{-/-}$ hESCs, EBs, and NPCs. Mean ± SD; n = 3 independent experiments; **p < 0.01, ***p < 0.001, ****p < 0.0001.

(D) TP53 ChIP-seq and RNA-seq tracks from the Integrative Genomics Viewer in the *BBS9* gene in WT hESCs and NPCs and in $TP53^{-/-}$ hESCs. TheTP53 ChIP-seq peaks in introns 9 and 14 are underlined. Assay for transposase-accessible chromatin using sequencing (ATAC-seq) and H3K27ac ChIP-seq tracks from previously published studies are also shown.
(E) qPCR analysis of the mRNA levels of *BBS9* in WT and $BBS9^{\Delta TP53BS1}$ hESCs and NPCs. Mean ± SD; n = 3 independent experiments; *p < 0.01, ***p < 0.001.
(F) Western blots of lysates of WT, $BBS9^{-/-}$, $BBS9^{\Delta TP53BS1}$, $CDKN1A^{-/-}/BBS9^{-/-}$, and $TP53^{-/-}$ NPCs with the indicated antibodies.

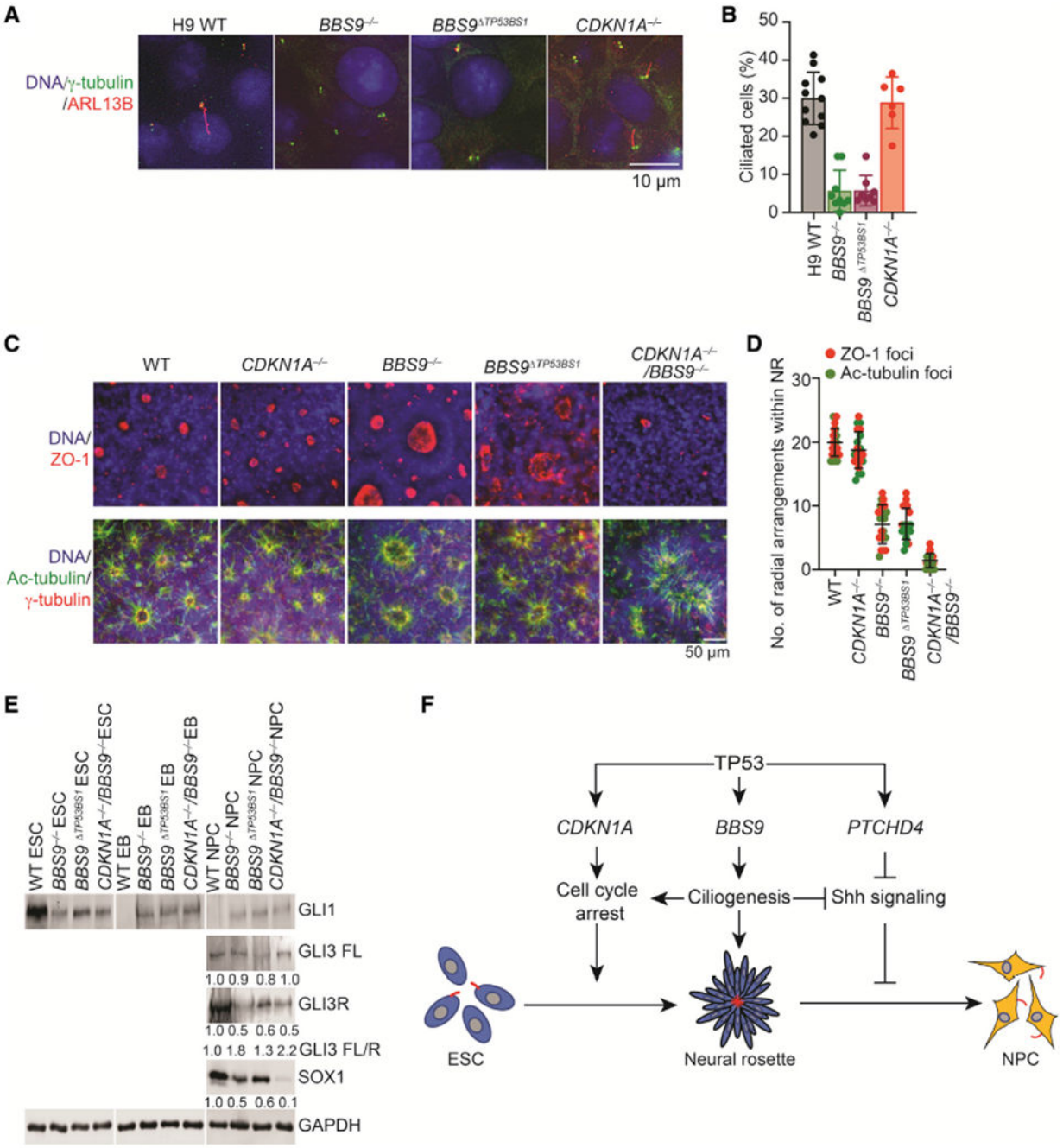

Figure 7. The TP53 target gene *BBS9* promotes ciliogenesis and NPC differentiation

(A) IF images of WT, *BBS9*$^{-/-}$, *BBS9*$^{\Delta TP53BS1}$, and *CDKN1A*$^{-/-}$ ESCs stained with DAPI for DNA (blue) and antibodies against ARL13B (red) and γ-tubulin (green).

(B) Quantification of the percentage of ciliated cells in (A). Each dot represents one field of view. Mean ± SD; n = 11 (total 695 cells) for WT; n = 9 (total 464 cells) for *BBS9*$^{-/-}$; n = 8 (total 639 cells) for *BBS9*$^{\Delta TP53BS1}$; n = 6 (total 542 cells) for *CDKN1A*$^{-/-}$.

(C) IF images of WT, *CDKN1A*$^{-/-}$, *BBS9*$^{-/-}$, *BBS9*$^{\Delta TP53BS1}$, and *CDKN1A*$^{-/-}$/*BBS9*$^{-/-}$ NRs stained with DAPI for DNA and the indicated antibodies. Top and bottom panels show different NRs of each cell line.

(D) Quantification of the number of radial arrangements (as defined by ZO-1 and Ac-tubulin foci) within each WT or the indicated mutant NR. Each dot represents one NR. Mean ± SD; n = 10 for ZO-1 and Ac-tubulin.

(E) Western blots of lysates of WT, *BBS9*$^{-/-}$, *BBS9*$^{\Delta TP53BS1}$, and *CDKN1A*$^{-/-}$/*BBS9*$^{-/-}$ ESCs, EBs, and NPCs with indicated antibodies. The relative intensities of GLI3 FL and GLI3R and their ratios are indicated.

(F) Functions of TP53 during hESC differentiation into NPCs. TP53 activates the expression of *CDKN1A* and *BBS9* to execute cell-cycle arrest and promote ciliogenesis, respectively. Both processes ensure the formation of tightly compacted NRs, which exert spatiotemporal control of Shh signaling. TP53 also activates the expression of *PTCHD4*, an inhibitor of Shh signaling. These mechanisms collectively suppress Shh signaling and promote NPC differentiation.

KEY RESOURCES TABLE

REAGENT or RESOUCE	SOURCE	IDENTIFIER
Antibodies		
Anti-SOX2-APC	Miltenyi Biotech	Cat#130-104-995; Clone REA320; RRID: AB_2653503
Anti-OCT3/4 Isoform A-PE	Miltenyi Biotech	Cat#130-105-606; clone: REA338; RRID: AB_2653084
Brilliant Violet 421™ anti-NANOG	Bio Legend	Cat#674208; Clone 16H3A48; RRID: AB_2566688
Rabbit polyclonal anti-ZO-1 antibody	Thermo Fisher Scientific	Cat#402200; RRID: AB_2533456
Rabbit polyclonal anti-SOX2 antibody	Abcam	Cat#ab97959; RRID: AB_2341193
Mouse monoclonal anti-NANOG antibody	Thermo Fisher Scientific	Cat#MA1017; Clone 23D2-3C6; RRID: AB_2536677
Rabbit polyclonal anti-OCT3/4 antibody	Santa Cruz Biotechnology	Cat#sc-9081; Clone H134; RRID: AB_2167703
Rabbit polyclonal anti-SOX1 antibody	Cell Signaling Technology	Cat#4194S; RRID: AB_1904140
Rabbit polyclonal anti-Ki67 antibody	Abcam	Cat#ab15580; RRID: AB_443209
Rabbit polyclonal anti-g Tubulin antibody	Abcam	Cat#ab11317; RRID: AB_297921
Mouse monoclonal anti-Tubulin acetylated antibody	Sigma-Aldrich	Cat#T6793; Clone 6-11B-1; RRID: AB_477585
Rabbit polyclonal anti-ARL13B antibody	Proteintech	Cat#17711-1-AP; RRID: AB_2060867
Rabbit monoclonal anti-SALL4	Abcam	Cat#ab226756; clone SP289; RRID: AB_2904128
Rabbit polyclonal anti-GFAP	Abcam	Cat#ab7260; RRID: AB_305808
Rabbit monoclonal anti-Glypican-3 antibody	Abcam	Cat#207080; Clone EPR20569; RRID: AB_2904127
Mouse monoclonal anti-p53 antibody	Santa Cruz Biotechnology	Cat#sc-126; Clone DO-1; RRID: AB_628082
Mouse monoclonal anti-p53 antibody	Santa Cruz Biotechnology	Cat#sc-98; Clone Pab 1801; RRID: AB_628085
Rabbit polyclonal anti-p53 antibody	Sigma-Aldrich	Cat#SAB4503011; RRID: AB_10748209
Rabbit monoclonal anti-GAPDH antibody	Cell Signaling Technology	Cat#2118; Clone 14C10; RRID: AB_561053
Mouse monoclonal anti-OCT3/4 antibody	Santa Cruz Biotechnology	Cat#sc-5279; Clone C-10; RRID: AB_628051
Mouse monoclonal anti-NANOG antibody	Santa Cruz Biotechnology	Cat#sc-293121; Clone 1E6C4; RRID: AB_2665475
Rabbit polyclonal anti-BBS9 antibody	Sigma-Aldrich	Cat#HPA021289; RRID:AB_1845286
Mouse monoclonal anti-g Tubulin antibody	Sigma-Aldrich	Cat#T6557; Clone GTU-88; RRID:AB_477584
IRDye 800CW Donkey anti-Goat IgG (H+L)	Licor Biosciences	Cat#926-32214; RRID:AB_621846
Anti-rabbit IgG Dylight 800 Conjugate	Cell Signaling Technology	Cat#5151; RRID:AB_10697505
Anti-mouse IgG Dylight 680 Conjugate	Cell Signaling Technology	Cat#5470; RRID:AB_10696895
Donkey anti-rabbit Alexa Fluor antibody	Thermo Fisher Scientific	Cat#A-21206; RRID:AB_2535792
Chemicals, peptides, and recombinant proteins		
Matrigel hESC-qualified matrix, LDEV free	Corning	Cat#354277
mTeSR1-cGMP	Stem Cell Technologies	Cat#85850
Versene solution	Thermo Fisher Scientific	Cat#15040066
Puromycin Dihydrochloride	Thermo Fisher Scientific	Cat#A1113803
Lipofectamine 2000	Thermo Fisher Scientific	Cat#11668019
Lenti-X Concentrator	Takara Bio	Cat#631232

REAGENT or RESOUCE	SOURCE	IDENTIFIER
Trypan Blue Stain (0.4%)	Thermo Fisher Scientific	Cat#T10282
DAPI	Sigma-Aldrich	Cat#D9542-10MG
Reversine	Sigma-Aldrich	Cat#R3904-5MG
Hoechst 33342, Trihydrochloride, Trihydrate	Thermo Fisher Scientific	Cat#H3570
Aphidicolin	Sigma-Aldrich	Cat#A0781-10MG
Paraformaldehyde	Sigma-Aldrich	Cat#158127-500G
DMEM	Thermo Fisher Scientific	Cat#11965-118
BSA	Sigma-Aldrich	Cat#A7906-100G
Vectashield mounting medium	Vector Laboratories	Cat#H-1000
VWR Formalin- 10% neutral buffered	VWR	Cat#16004-126
Citrate buffer, pH 6.0	Sigma-Aldrich	Cat#C9999
Hydrogen peroxide 30%	Sigma-Aldrich	Cat#H3410
Accutase	StemCell Technologies	Cat#07920
Y-27632 Rho/Rock pathway Inhibitor	StemCell Technologies	Cat#72308
StemDiff Neural Rosette Selection reagent	StemCell Technologies	Cat#05832
StemDiff Neural Progenitor Medium	StemCell Technologies	Cat#05833
BD phosflow Perm buffer II and III	BD Biosciences	Cat#558050
Glycoblue Coprecipitant	Thermo Fisher Scientific	Cat#AM9515
Critical commercial assays		
StemDiff SMADi Neural induction kit	StemCell Technologies	Cat#08582
AggreWell 800 plate starter kit	StemCell Technologies	Cat#34850
TruSeq Stranded mRNA Library Preparation Kit	Illumina	Cat# 20020594
DNeasy Blood & Tissue kit	Qiagen	Cat#69506
Human GeCKO v2 library	Addgene	Cat#1000000048
Qubit DNA BR assay kit	Thermo Fisher Scientific	Cat#Q32853
Qubit DNA HS assay kit	Thermo Fisher Scientific	Cat#Q32854
Qubit RNA BR assay kit	Thermo Fisher Scientific	Cat#Q10210
Deposited data		
All raw and analyzed RNA-seq, ChIP-seq and CRISPR-Cas9 screen data	This manuscript	GEO: GSE168587
Published H3K27ac ChIP-seq and chromatin accessibility data	Ziller et al., 2015; http://cistrome.org/	GEO: GSM1521726; GSM2386581
Experimental models: Cell lines		
H1 human embryonic stem cell line (hESC)	Wicell Research Institute	WA01
H9 hESC	Wicell Research Institute	WA09
293FT Cell Line	Thermo Fisher Scientific	R70007
Experimental models: Organisms/strains		
NOD.Cg-*Prkdc*^{scid}/J (NOD SCID)	The Jackson Laboratories	Strain#001303; Sex: Female
Oligonucleotides		
TP53 sgRNA#1: AAGGGACAGAAGATGACAG	This manuscript	N/A

REAGENT or RESOUCE	SOURCE	IDENTIFIER
TP53 sgRNA#2: TGAAGCTCCCAGAATGCCAG	This manuscript	N/A
TP53 sgRNA#3: TCGACGCTAGGATCTGACTG	This manuscript	N/A
IFT140 sgRNA: TACCCCGATCCTTAAACGTC	This manuscript	N/A
OFD1 sgRNA: CCGACATCACCGTGCTCCGT	This manuscript	N/A
CDKN1A sgRNA#1: GGAGAAGATCAGCCGGCGTT	This manuscript	N/A
CDKN1A sgRNA#2: ACTCTCAGGGTCGAAAACGG	This manuscript	N/A
BBS9 sgRNA#1: AGTTCTCGAGATTGAACGTT	This manuscript	N/A
BBS9 sgRNA#2: TGATTCTGCTGATCGCGCTG	This manuscript	N/A
BBS9 sgRNA#3: CTGAAGGTAAGATTTCACCT	This manuscript	N/A
BBS9 sgRNA#4: ACGCAGATATGGCTGAACTA	This manuscript	N/A
Recombinant DNA		
Plasmid pSpCas9(BB)-2A-GFP (PX458)	Addgene	Plasmid #48138
Plasmid pSpCas9(BB)-2A-Puro (PX459) V2.0	Addgene	Plasmid #62988
LentiCRISPR v2	Addgene	Plasmid #52961
Plasmid pMD2.G	Addgene	Plasmid #12259
Plasmid psPAX2	Addgene	Plasmid #12260
Plasmid pWPI-p53	This manuscript	N/A
Software and algorithms		
R Development Core	N/A	https://www.r-project.org
FastQC	N/A	http://www.bioinformatics.babraham.ac.uk/projects/fastqc
FastQ Screen	N/A	http://www.bioinformatics.babraham.ac.uk/projects/fastq_screen
fastq-m*cf.*	Aronesty (2013)	https://github.com/ExpressionAnalysis/ea-utils/blob/wiki/FastqMcf.md
Picard tools	N/A	https://broadinstitute.github.io/picard/
featureCounts	Liao et al. (2014)	http://bioinf.wehi.edu.au/featureCounts/%20
TMM	Robinson et al. (2010)	N/A
edgeR	Huang da et al. (2009)	https://bioconductor.org/packages/release/bioc/html/edgeR.html
ComplexHeatmap	Gu et al. (2016)	https://www.bioconductor.org/packages/release/bioc/html/ComplexHeatmap.html
ChIPseeker	Yu et al. (2015)	https://bioconductor.org/packages/release/bioc/html/ChIPseeker.html
Bowtie2	Langmead and Salzberg (2012)	http://bowtie-bio.sourceforge.net/bowtie2/index.shtml
HOMER	Heinz et al. (2010)	http://homer.ucsd.edu/homer/ngs/peakMotifs.html
BEDTools	Quinlan and Hall (2010)	https://bedtools.readthedocs.io/en/latest/content/tools/intersect.html
STAR	Dobin et al. (2013)	https://github.com/alexdobin/STAR
GSEA	Mootha et al. (2003) and Subramanian et al. (2005)	N/A
TSEA	Wells et al. (2015)	http://genetics.wustl.edu/jdlab/tsea/

REAGENT or RESOUCE	SOURCE	IDENTIFIER
BWA	Li (2013)	http://bio-bwa.sourceforge.net/
HMM copy	Lai and Shah (2016)	https://bioconductor.org/packages/release/bioc/html/HMMcopy.html
MAGeCK	Li et al. (2014)	https://sourceforge.net/p/mageck/wiki/Home/
Prism9	GraphPad	https://www.graphpad.com/scientific-software/prism/
Adobe Illustrator	Adobe	https://www.adobe.com/products/illustrator.html
Fiji	ImageJ	https://imagej.net/software/fiji/
Metamorph imaging software	Molecular Devices	N/A
Other		
37mm reversible strainer	StemCell Technologies	Cat#27215
Leica inverted microscope equipped with environmental chamber	Leica Biosystems	N/A
Deltavision microscope	GE Healthcare	N/A
Leica Aperio CS2 Slide Scanner	Leica Biosystems	N/A
Odyssey infrared imaging system	LI-COR Biosciences	N/A
Lonza 4D-Nucleofector	Lonza Biosciences	N/A
Bio-Rad TC20 automated cell counter	Bio-Rad	N/A
Beckman Coulter CytoFLEX flow cytometer	Beckman Coulter Life Sciences	N/A
NextSeq 500 high output sequencer	Illumina	N/A